Vol. 2 , No. 3-4 , July-October , 2006

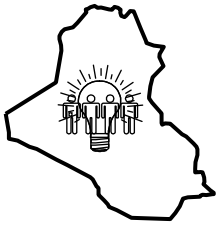

SPONSORED AND PUBLISHED BY
THE IRAQI SOCIETY FOR ALTERNATIVE AND RENEWABLE ENERGY SOURCES AND TECHNIQUES (I.S.A.R.E.S.T.)

EDITORIAL BOARD

ADVISORY BOARD

Organized by I.S.A.R.E.S.T.

INVITATION TO PARTICIPATE

WHAT IS ENERGY?

Energy is neither created nor destroyed. This is called the principle of Conservation of Energy. In other words, the amount of energy in the universe always remains the same. And when we use energy, like burning wood to generate light and heat, we don't use it up; we simply transform it from one form of potential energy (fuel) into other forms of kinetic energy (heat and light).

Almost all energy transformations involve the production of heat, which is considered the lowest form of energy, because it quickly dissipates into the surroundings and is normally unavailable for further use. So, although the total amount of energy remains the same, the amount of "useable" energy constantly decreases. However, don't worry too much about the decrease of useable energy; our Sun is scheduled to produce solar energy for many years to come, so taking this course will not be a waste of your time (or energy).

Energy is all around us. It heats our homes, powers our light bulbs and appliances, fuels our cars and provides for a variety of professional careers that deal with its many elements. It also comes in many forms such as heat, light, chemical, mechanical and electrical energy. And, according to physicists, energy can neither be created nor destroyed, only converted from one form to another. So why learn about energy? The answer is because energy, and the conversion of energy from one form to another, is fundamental to our modern living environment. By knowing the principles behind energy generation and conversion, you will come away with a knowledge base that can be applied to nearly every modern electrical, mechanical and chemical device that uses or produces power.

To introduce more about the alternative and renewable energy sources and techniques, I.S.A.R.E.S.T. invites you to attend the scientific lectures organized by I.S.A.R.E.S.T. You are requested to contact the secretary of the society and register your attendance. The lectures can be held earlier due to the registered requests.

To all they would like to submit seminars or scientific lectures during the third semester of the **I.S.A.R.E.S.T.** (July, August and September) in 2006, you are kindly requested to contact the secretary of the **I.S.A.R.E.S.T.** for date and presentation arrangements of the seminars or lectures. Please, do not hesitate to participate in our activities, this chance might be required by young scientists in our country, IRAQ, to develop and grow as well as introduce the professors and experts in field. You could find us on the post address, emails and mobile below:

Mailing Address:

P. O. Box 55259, Baghdad 12001, IRAQ

Emails:

irq_appl_phys@yahoo.com

editor_ijap@yahoo.co.uk

odayata2001@yahoo.com

Mobile:

00964-7901274190

M. Kourogi
B. Widiyatmoko
K. Imai
T. Shimizu
M. Ohtsu

Tokyo Institute of Technology, Nagatsuta, Midori-ku, Yokohama, Japan

Accurate Relative Frequency Cancellation Between Two Independent Lasers

For high-precision frequency-based applications of lasers, the frequency difference between two independent lasers is accurately stabilized and maintained. We describe a simple and novel feed-forward method with an acousto-optic modulator. This method can be used in optical phase-locked loops.

***Keywords*: Frequency cancellation, Laser applications, Pulse locking**

High-precision frequency-based applications of lasers, such as optical frequency and pulse synthesis and frequency chains for measurement of stable optical frequency reference and optical communications, require precise optical frequency locking. An optical phase-locked loop[1,2] (OPLL) has been used as a key element for this purpose. An OPLL can be used to reduce relative laser frequency fluctuations as low as 1 mHz. For example, an OPLL is necessary for each conversion from one intermediate frequency to another intermediate frequency in an optical frequency chain. A frequency chain based on optical frequency divider stages[3] requires many OPLL's. A subfemtosecond pulse can be synthesized by use of separate phase-locked laser oscillators.[4] OPLL's are also used for optical transmission systems.[5]

However, there are some problems connected with use of such OPLL's. The performance of an OPLL is extremely sensitive to the frequency response of the laser and to the delay time in the feedback loop.[6] When an OPLL is used for a laser such as a semiconductor laser with a large amount of frequency-modulation noise, high-speed control is necessary for phase locking.[7] The frequency-modulation characteristics of some lasers might not be suitable for high-speed control. When the amplitude of the residual phase noise in the phase-locked condition exceeds the dynamic range of the phase detector of the OPLL, it induces a cycle slip[8] in the OPLL.

In this Letter we describe a simple and effective technique for precise optical relative frequency locking. This method can be used in an optical phase-locked loop to lock two lasers. Because this technique is based on feed-forward cancellation of frequency and phase fluctuation between two lasers, it is not sensitive to the frequency response of the laser or to the delay time in the loop. The technique bears a similarity to those used in cancellation of phase noise introduced by an optical fiber in an experiment of Ma *et al.*[9] and in a phase-locked loop proposed by Nishikido and Himeno.[10] However, the technique is fundamentally different in two respects: (1) it is used for relative frequency cancellation between two independent lasers and (2) it is based on a feed-forward control.

The concept that underlies our relative frequency cancellation is to use a frequency shifter directly driven by a beat signal between two lasers. To control the frequency (ν_S) of a slave laser (LD S; Fig. 1) to that (ν_M) of a master laser (LD M) we shift the frequency

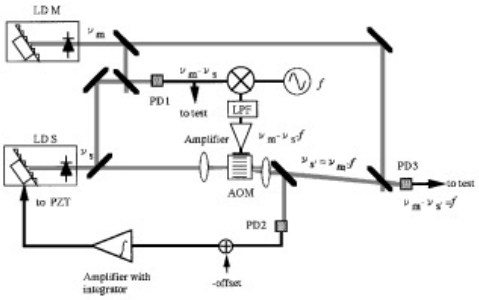

Fig. 1. Experimental setup: LPF, low-pass filter; other abbreviations defined in text.

of LDS by the beat frequency ($\nu_M - \nu_S$) between the two lasers. Thus the resultant frequency (ν_S') of LDS is equal to $\nu_S + (\nu_M - \nu_S) = \nu_M$. This means that the relative frequency is canceled and the frequency of LDS becomes that of LDM. In other words, ν_S is locked to ν_M without use of the feedback control of the light source. It is also expected that the phase information of LDM will be transferred to LDS because the relative phase information between the two lasers is perfectly included in the heterodyne beat signal.

To study this frequency-cancellation concept experimentally we used the setup shown in Fig. 1. The heterodyne beat (frequency = $\nu_M - \nu_S$) between two single-frequency 1.5-μm laser diodes with external gratings was formed in a photodetector (PD1). To facilitate precise rf measurements we mixed the beat signal from PD1 with the signal from a frequency synthesizer (frequency f) in a double-balanced mixer and then amplified one of the intermediate frequencies (frequency $\nu_M - \nu_S - f$) from the double-balanced mixer to 0.5 W to drive a $LiNbO_3$ acousto-optic frequency modulator (AOM). Higher harmonics were rejected with a low-pass filter. Thus the light-diffracted frequency from the AOM is $\nu_M - f$.

The direction of the diffracting light beam from the AOM changes for different input beat frequencies. To minimize the effect of the changes in the direction of diffraction, we focused the incident laser light in the AOM, which also effectively reduced the traversal time of the acoustic wave through the laser beam, which determines the modulation bandwidth of the AOM. (The modulation bandwidth of AOM should be much larger than the linewidth of the lasers to yield a small phase error in the frequency cancellation.) Furthermore, to correct the long-term drift we detected the position of the beam of the AOM output with photodiode PD2 located off the axis of the laser beam; then the error signal was fed back to a piezoelectric transducer (PZT) on which the grating of LDS was mounted. This control maintained the frequency $\nu_M - \nu_S - f$ in a range of several megahertz from 80-MHz driving frequency. (Without this additional servo the laser cannot stay in lock for more than 10 min.)

Figure 2 shows the spectral density of the beat signal in photodetectors PD1 and PD3 observed with a rf spectrum analyzer. Curve A of Fig. 2(a) shows the spectrum measured with PD1, i.e., the beat signal between two lasers whose center frequencies were locked with PD2. The measured spectrum includes the natural linewidths and acoustic fluctuations of the two lasers. Curve B of Fig. 2(b) shows the spectrum measured with PD3, i.e., the beat signal under an auxiliary controlled condition. The resolution bandwidth was 3 kHz. From this figure it can be seen that the center frequency is f (=120 MHz); the delta function is seen at the center, and the width is equal to the analyzer resolution bandwidth. This is the evidence that short-term control is efficient. An oscillatory shape is seen in the wings of the power spectrum because the delay time τ of the AOM is much smaller than the laser's coherence time and is much larger than the traversal time of the acoustic wave through the laser beam.

Our calculation of the power spectrum is shown as curve C of Fig. 2(b), where τ is assumed to be 1 μs. The method of the calculation was similar to that of self-delay heterodyne linewidth measurement.[11] The results of our calculation agree with the experimental results. The time-delay effect limits the decrease of the noise level in the wings of the power spectrum. The noise level in the wings may be a serious problem, depending on applications. The calculation of the power spectrum is shown by curve D of Fig. 2(b) when the delay time is assumed to be 0.1 μs. From this curve we expect that the level of the wings of the power spectrum will be reduced for a decreased delay time. Therefore we can expect that, if the effect of the delay time is compensated for, the level of the wings of the power spectrum can be decreased. The effect of the delay time can be compensated for by insertion of an optical delay line between LDS and the AOM. An optical fiber with a length corresponding to the delay time can be used as the optical delay line. Furthermore, if limitations arise from acoustic group-velocity dispersion, they can also be compensated for by use of a circuit with an inverted group velocity.

To obtain an accurate time-domain measurement, we used a frequency counter to measure the heterodyne beat in PD3. The measured Allan deviation is shown in Fig. 3. It reaches 1 mHz in an average time period of 1000 s, equivalent to a millihertz accuracy level for the cancellation. This accuracy is comparable with the level of an OPLL. We believe that this method should be able to be used in an OPLL. Further, by improving

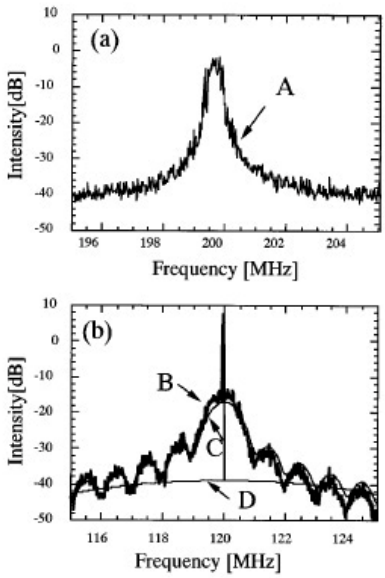

Fig. 2. Optical field spectral profile of the beat signal: A, measured with PD1; B, measured with PD3; C, calculation of B when the delay time is 1 μs; D, calculation when the delay time is decreased to 0.1 μs. The analysis bandwidth is 3 kHz.

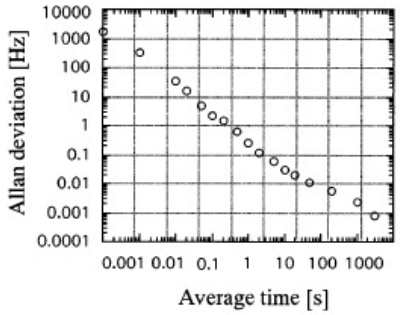

Fig. 3. Allan deviation of the beat signal measured with PD3.

the circuits for dividing a beat frequency into halves, we can also apply this method to an optical divider stage in which a laser is stabilized to the mean of two laser frequencies.

In summary, with the combination of an acousto-optic modulator and a simple demonstration setup, we have shown that the system that we designed cancels the frequency fluctuation between two independent lasers with millihertz accuracy. This method can be used in optical phase-locked loops.

References

1. L. H. Enloe and J. L. Rodda, Proc. IEEE **53,** 165 (1965).
2. H. R. Telle and H. Li, Electron. Lett. **26,** 858 (1990).
3. H. R. Telle, D. Meschede, and T. W. Hänsch, Opt. Lett. **15,** 532 (1990).
4. T. W. Hänsch, Opt. Commun. **80,** 71 (1990).
5. J. M. Kahn, IEEE Photon. Technol. Lett. **1,** 340 (1989).
6. M. A. Grant, W. C. Michie, and M. J. Fletcher, J. Lightwave Technol. **LT-5,** 592 (1987).
7. M. Kourogi, C. H. Shin, and M. Ohtsu, IEEE Photon. Technol. Lett. **3,** 270 (1991).
8. G. Ascheid and H. Meyr, IEEE Trans. Commun. **COM-30,** 2228 (1982).
9. L.-S. Ma, P. Jungner, J. Ye, and J. L. Hall, Opt. Lett. **19,** 1777 (1994).
10. J. Nishikido and A. Himeno, in *Photonic Switching II, Proceedings of the International Topical Meeting*, K. Toda and H. S. Hinton, eds. (Springer-Verlag, Berlin, 1990), p. 274.
11. L. E. Richther, H. I. Mandelberg, M. S. Kruger, and P. A. McGrath, J. Quantum Electron. **QE-22,** 2070 (1986).

Gregory J. Wagner
Timothy J. Carrig
Ralph H. Page
Kathleen I. Schaffers
Jean-Oliver Ndap
Xiaoyan Ma
Arnold Burger

Coherent Technologies, Inc., Lafayette, Colorado, U.S.A

Continuous-Wave Broadly Tunable Cr^{2+}:ZnSe Laser

We report room-temperature operation of an all-solid-state broadly tunable continuous-wave Cr^{2+}:ZnSe laser. Output power of 250mW, an absorbed power slope efficiency of 63%, and continuous tunability from 2138 to 2760 nm are demonstrated.

***Keywords*: Cr^{2+} laser, Tunable lasers, Solid-state lasers**

Broadly tunable laser sources in the 2–4-μm spectral region are of interest for a variety of scientific and remote-sensing applications. Demonstrated continuous-wave (cw) broadly tunable sources in this wavelength range include the Tm:YLF laser,[1] color-center lasers, lead-salt diode lasers, gas and chemical lasers, and optical parametric oscillators. However, these devices often suffer from disadvantages such as cryogenic operation, complexity, narrow-band or discontinuous tuning, and limited routes to power scaling. Recently, Cr^{2+}-doped chalcogenide crystals have been proposed as highly efficient room-temperature alternatives to these sources.[2,3] Pulsed lasing of Cr^{2+}:ZnSe,[2,4] Cr^{2+}:ZnS,[4] Cr^{2+}:CdSe,[5] and Cr^{2+}:CdMnTe[6,7] has been demonstrated. In this Letter we describe room-temperature operation of a cw Cr^{2+}:ZnSe laser that operates with high efficiency, is broadly and continuously tunable from 2138 to 2760 nm, and can be directly diode pumped.[4] To the best of our knowledge, this is the first reported cw lasing of a transition-metal-doped chalcogenide crystal and the broadest wavelength tuning yet demonstrated from any room-temperature cw laser.

Cr^{2+}:ZnSe is attractive for room-temperature cw laser applications because of a near-unity fluorescence quantum efficiency at 300 K, a high gain cross section ($\sigma_{emis} \sim 9 \times 10^{-19}$ cm^2), and extremely wide vibronically broadened absorption and emission bands.[2] Additionally, the Cr^{2+} ion in the ZnSe host effectively has a two-term electronic structure (transitions to higher-lying levels are spin forbidden and, presumably, very weak) that precludes losses that are due to excited-state absorption or upconversion but allows four-level laser action.

In this study polished Cr:ZnSe crystals with thicknesses in the 1–3-mm range were used. Absorption at the pump wavelength varied from approximately 30% to 100%, depending on the sample. All laser crystals were prepared by use of diffusion doping.[4,8]

Initial laser experiments were conducted with a three-mirror folded resonator, shown in Fig. 1, consisting of 5- and 10-cm radius-of-curvature high reflectors and a plano output coupler. The resonator length was 36.5 cm. The laser crystal was clamped between two small room-temperature copper blocks and placed at Brewster's angle between the curved mirrors. The Cr:ZnSe crystal was not actively cooled. The resonator formed a cavity waist ($1/e^2$ radius) of approximately 65 μm in the laser crystal. The pump source was a cw diode-pumped Tm:YALO laser[9] operating at approximately 1940 nm with a nominal output power of 1 W in a TEM_{00} mode. The pump beam was focused to a 60-μm radius spot in the Cr:ZnSe crystal. Use of a gold-coated cavity end mirror resulted in double-pass pumping of the laser crystal. A variable attenuator, consisting of a calcite polarizer and a half-wave plate, was used to vary the pump power without changing the pump-beam alignment or spatial profile.

Our best laser crystal was 2.76 mm thick and had a single-pass absorption of approximately 35% at the pump wavelength. By double passing the pump

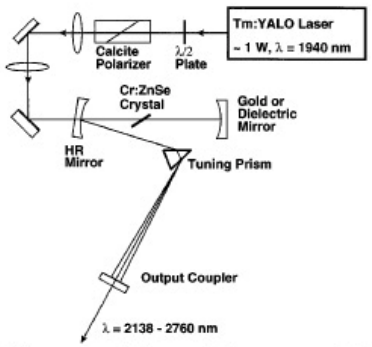

Fig. 1. Schematic of the optical system and the laser cavity used for most of the Cr:ZnSe laser experiments. The Cr:ZnSe laser is pumped by a 1-W diode-pumped Tm:YALO laser. No tuning elements were present during slope-efficiency measurements. HR, high reflector.

beam through the Cr:ZnSe crystal, we were able to increase the total pump absorption to approximately 58%. Knife-edge scans of the double-passed pump beam showed that good mode matching was maintained. The estimated Cr^{2+} concentration in the crystal was 2.6×10^{18} cm^{-3}. At room temperature the peak-to-$1/e$ fluorescence decay time was measured to be 6.8 ± 0.5 μs for this crystal, although we note that lifetime measurements varied by several microseconds among different crystal samples.

By use of a 7% output coupler, a cw output power of 250 mW from the Cr:ZnSe laser was achieved with double-pass pumping. Figure 2 shows a plot of the laser output power as a function of absorbed pump power. An absorbed power slope efficiency of 63% was measured. The laser produced a TEM_{00} spatial mode and had a free-running linewidth of approximately 50 nm (FWHM), centered at 2400 nm. This linewidth is approximately the same as that observed in pulsed Cr:ZnSe and Cr:CdMnTe lasers.[4,10] Using a 1% output coupler, we observed absorbed power thresholds as low as 140 mW.

To quantify the passive loss of our best laser crystal, we applied three measurement techniques. The first approach was to pass a probe beam from a second Cr:ZnSe laser through the unpumped Cr:ZnSe laser crystal and directly measure the single-pass loss. A value of 2% was obtained.

The second and third approaches involved making absorbed power threshold and slope-efficiency measurements by use of three different output couplers and then applying a traditional Findlay–Clay analysis[11] or generating a Caird plot.[12] The nominal output coupler reflectivities used were 99%, 97%, and 93%. Figure 3 shows laser output power plotted as a function of absorbed pump power for the three output couplers. To eliminate any error owing to imperfect mode overlap of the second pass of the pump beam through the laser crystal, we replaced the gold cavity end mirror with a dielectric mirror that was highly transmissive at the pump wavelength. This resulted in single-pass pumping and, correspondingly, lower output power than is shown in Fig. 2.

The Findlay–Clay analysis consists of plotting threshold pump power versus the natural log of the output coupler reflectivity and then extrapolating a linear curve fit to the data to determine round-trip cavity loss. This yields a single-pass cavity loss value of approximately 4.5%.

The Caird plot is created by means of plotting inverse absorbed power slope efficiency ($1/\eta_{abs}$) versus inverse output coupling ($1/T$). An advantage to this approach is that both the round-trip cavity loss (L) and the intrinsic slope efficiency (η_0) are calculated. When we apply the relation

$$1/\eta_{abs} = 1/\eta_0 + (L/\eta_0)(1/T) \quad (1)$$

to the data, the slope of the linear curve fit is equal to L/η_0 and the y-axis intercept is equal to $1/\eta_0$. Solving this equation yields an intrinsic slope efficiency of 68% and a round-trip cavity loss of 1.5% (single-pass loss of 0.75%). For both the Findlay–Clay and the Caird plot analyses, the single-pass loss values are interpreted as being approximately equal to the passive loss of the Cr:ZnSe crystal.

The three measurements of crystal single-pass loss resulted in values of 0.75%, 2%, and 4.5%. These numbers agree reasonably well. Their differences can be attributed to measurement approximations (such as assuming a unity pumping efficiency and perfect mode matching of the pump and cavity modes), amplitude noise in the probe beam, thermal fluctuations in the detector, and the lack of linearity in the output power curves shown in Fig. 3. Furthermore, the change in laser slope efficiencies observed near threshold may indicate that localized heating effects are present in the passively cooled ZnSe crystal. Thermal effects are expected to be pump-power dependent and will perturb

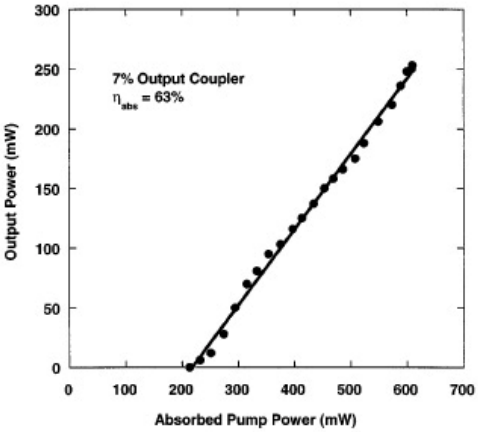

Fig. 2. Cr:ZnSe laser output power as a function of absorbed pump power. A gold-coated cavity end mirror was employed, resulting in double-pass pumping. The absorbed pump-power slope efficiency was 63%.

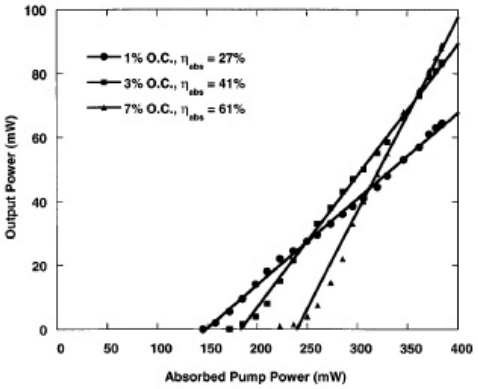

Fig. 3. Cr:ZnSe laser output power as a function of absorbed pump power. The cavity end mirror was highly transmissive at the pump wavelength, resulting in single-pass pumping of the laser crystal. The slope efficiencies are calculated from linear fits to the data. O.C., output coupler.

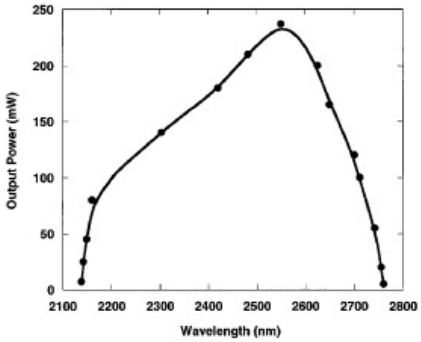

Fig. 4. The Cr:ZnSe laser was tuned with an intracavity Brewster-cut prism, resulting in continuous tunability from 2138 to 2760 nm. Output power of greater than 50 mW was maintained over a 600-nm-wide tuning range by use of a single set of cavity optics.

laser operation (for instance, changes in fluorescence lifetime, thermal lensing in the gain medium, and system alignment are expected). It is noteworthy that all three measured passive loss values are low relative to values reported in the literature.[4]

For a laser wavelength of 2400 nm and a pump wavelength of 1940 nm, the quantum-defect-limited slope efficiency is 81%. The difference between this value and the calculated intrinsic slope efficiency of 68% is reasonable given the described sources of measurement error. Importantly, the Caird plot measurement[12] indicates that excited-state absorption does not play a significant role in this material.

By use of a ZnSe output coupler and a ZnSe Brewster tuning prism, the Cr:ZnSe laser was tuned continuously from 2138 to 2760 nm, with a linewidth of approximately 30 nm (FWHM) and peak emission at 2550 nm, as shown in Fig. 4. The linewidth narrows to less than 10 nm (FWHM) at the ends of the tuning curve. An absorption spectrum of the Cr:ZnSe laser crystal and the reflectivities of the cavity optics were measured with a Cary 5E spectrophotometer. These data and the absorption cross-section values[2] were then used to model the absorbed power threshold as a function of wavelength for the Cr:ZnSe laser. The model indicates that the tuning range is limited primarily by ground-state absorption in the Cr:ZnSe crystal at shorter wavelengths and by the coatings of the cavity optics at longer wavelengths. The use of lower-concentration doped Cr:ZnSe crystals may allow tuning to wavelengths shorter than 2138 nm, and the use of broadband mirror coatings could potentially increase the upper tuning limit beyond 2760 nm.

To narrow the laser linewidth, we inserted an uncoated 75-μm-thick borosilicate etalon into the prism-tuned cavity. This resulted in an output spectrum consisting of two separate emission peaks, located at 2540 and 2572 nm, when the laser was tuned for maximum output power. Each peak had a FWHM of less than 4 nm. With the available etalons, we were unable to narrow the linewidth further or force the laser output into a single emission line. However, with appropriate optics it should be straightforward to achieve narrow-linewidth single-wavelength operation.

In conclusion, a highly efficient, broadly tunable cw laser source has been demonstrated. The Cr:ZnSe laser exhibits a 622-nm-wide continuous tuning range extending from 2138 to 2760 nm, a low absorbed pump-power threshold of 140 mW, and room-temperature slope efficiencies as high as 63%. Potential applications include high-resolution spectroscopy, μ-Doppler or vibration measurements of hard targets, and injection seeding of pulsed laser sources for remote sensing of chemical species. Additionally, the broad emission bandwidth indicates that the laser should be suitable for ultrashort pulse generation. Future research will investigate laser power scaling, optimization of crystal thickness and doping concentration, a comparison of different crystal preparation techniques, and improved understanding of material properties.

Coherent Technologies, Inc., portions of this material are based on work supported by National Science Foundation grant DMI-9761589. Fisk University work was supported by NASA grants NCC8-133 and NCC8-145 and by U.S. Department of Energy grant DE-FG03-94SF20368.

References

1. J. F. Pinto, L. Esterowitz, and G. H. Rosenblatt, Opt. Lett. **19,** 883 (1994).
2. L. D. DeLoach, R. H. Page, G. D. Wilke, S. A. Payne, and W. F. Krupke, IEEE J. Quantum Electron. **32,** 885 (1996).
3. K. Schepler, S. Kuck, and L. Shiozawa, J. Lumin. **72–74,** 116 (1997).
4. R. H. Page, K. I. Schaffers, L. D. DeLoach, G. D. Wilke, F. D. Patel, J. B. Tassano, S. A. Payne, W. F. Krupke, K.-T. Chen, and A. Burger, IEEE J. Quantum Electron. **33,** 609 (1997).
5. J. McKay, K. Schepler, and S. Kuck, paper ThGG1 presented at the 1998 Optical Society of America Annual Meeting, Baltimore, Md., October 4–9, 1998.
6. J. T. Seo, U. Hommerich, S. B. Trivedi, R. J. Chen, S. Kutcher, and K. Grasza, in *Conference on Lasers and Electro-Optics*, Vol. 6 of 1998 OSA Technical Digest Series (Optical Society of America, Washington, D.C., 1998), paper CTuC3.
7. M. Turner, J. T. Seo, U. Hommerich, S. B. Trivedi, R. J. Chen, C. C. Wang, and S. Kutcher, paper ThGG2 presented at the 1998 Optical Society of America Annual Meeting, Baltimore, Md., October 4–9, 1998.
8. K.-T. Chen, T. D. Journigan, S. Lecointe, J. Tong, A. Burger, L. D. Deloach, R. H. Page, and S. A. Payne, presented at the Sixth Eastern Regional Conference on Crystal Growth, ACCG/East-95, Atlantic City, N.J., October 15–18, 1995.
9. R. C. Stoneman and L. Esterowitz, IEEE J. Quantum Electron. **1,** 78 (1995).
10. U. Hommerich, X. Wu, V. R. Davis, S. B. Trivedi, K. Grasza, R. J. Chen, and S. Kutcher, Opt. Lett. **22,** 1180 (1997).
11. D. Findlay and R. A. Clay, Phys. Lett. **20,** 277 (1966).
12. J. A. Caird, S. A. Payne, P. R. Staver, A. J. Ramponi, L. L. Chase, and W. F. Krupke, IEEE J. Quantum Electron. **24,** 1077 (1988).

Changxi Yang

Institute of Physics,
Chinese Academy of Sciences,
Beijing, China

Dispersion Compensation for a Femtosecond Self-Pumped Phase Conjugator

Dispersion compensation for a photorefractive self-pumped phase conjugator with femtosecond pulses is analyzed. The self-pumped phase conjugator consists of a pair of dynamic gratings coupled by total internal ref lections at the crystal surfaces (cat conjugator). The negative angular dispersions of refraction at the air–crystal interface and the gratings inside the crystal compensate for the positive dispersion of the finite crystal path. The experimental results show that with partial dispersion compensation the width of the self-pumped phase conjugation at 450 nm of femtosecond pulses is narrower than that of the transmitted pulses.

Keywords: **Femtosecond pulses, Phase conjugator, Dispersion**

Recently Yau *et al.*[1,2] fabricated a femtosecond photorefractive self-pumped conjugator. They observed that the self-pumped phase-conjugate pulses had a pulse width similar to that of the incident pulses at 797 nm. However, they did not analyze the dispersion of the femtosecond phase conjugator. Although Yariv *et al.*[3] proposed that the process of nonlinear optical phase conjugation could be utilized to compensate for channel dispersion, they discussed only the phase conjugation achieved by four-wave mixing in nondispersive media.

In this Letter we analyze the dispersion of the self-pumped phase conjugation of femtosecond pulses. The femtosecond self-pumped conjugation is generated in a cat mirror configuration. Without loss of generality we consider that the cat mirror consists of two interaction regions coupled by total internal reflections at the crystal faces[4] (Fig. 1). We neglect self-phase modulation. The pulse evolution is governed by group-velocity dispersion (GVD).[5] The phase conjugator can be represented by a complex optical transfer function in the frequency domain: $H(\Omega) = R(\Omega)\exp[-i\Psi(\Omega)]$, where $R(\Omega)$ is the amplitude response and $\Psi(\Omega)$ is the phase response.[6,7] We expand $\Psi(\Omega)$ at ω_l and obtain $\Psi(\Omega) = \sum_0^\infty b_n(\Omega - \omega_l)^n$ with the expansion coefficients

$$b_n = \frac{1}{n!}\frac{\mathrm{d}^n\Psi}{\mathrm{d}\Omega^n}\bigg|_{\omega_l}.$$

First we calculate the angular dispersions introduced by the air–crystal interface and the gratings inside the crystal. From Snell's law, the angular dispersion introduced by the air–crystal interface can be obtained:

$$\frac{\mathrm{d}\alpha}{\mathrm{d}\lambda} = -\frac{\sin\theta}{n(n^2 - \sin^2\theta)^{1/2}}\left(\frac{\mathrm{d}n}{\mathrm{d}\lambda}\right), \tag{1}$$

where n is the crystal's refractive index and θ and α are the angles of incidence and refraction, respectively.

We consider only the transmission gratings formed by the center frequency component ω_l of the incident pulse in the two interaction regions, A and E. We assume that $OA = l_1$ and $ABDE = l_2$. The grating spacing is $\Lambda = \lambda_l/(2n\sin\Theta/2)$, where Θ is the angle between the refraction beam and the fanning beam. The angular dispersion introduced by the transmission gratings is

$$\frac{\mathrm{d}\Theta}{\mathrm{d}\lambda} = \frac{1}{[(2n\Lambda)^2 - \lambda^2]^{1/2}}\left(1 - \frac{\lambda}{n}\frac{\mathrm{d}n}{\mathrm{d}\lambda}\right). \tag{2}$$

The diffraction beam from the grating in region A propagates a distance l_2 to reach interaction region E and undergoes two total internal reflections, at B and D. The two total internal reflections cause two phase changes. The dependence of the phase change on the

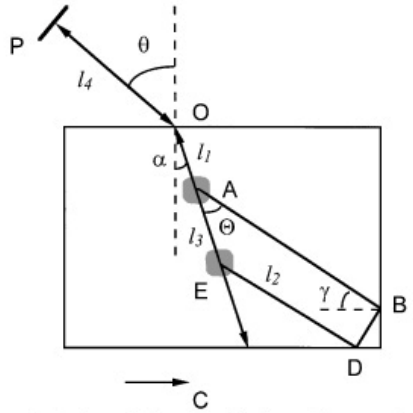

Fig. 1. Optical path loop inside the self-pumped phase conjugator. Two transmission gratings, in regions A and E, are formed by the center frequency components ω_l of the incident pulse. P is the observation plane, θ and α are the angles of incidence and refraction, respectively, and Θ and γ are the angles between the fanning beam and the refraction beam and the normal of the crystal surface. $OA = l_1$, $ABDE = l_2$, $EA = l_3$, $OP = l_4$.

wavelength at B is given by

$$\Phi_B = 2\tan^{-1}\frac{n(n^2\sin^2\gamma - 1)^{1/2}}{\cos\gamma}, \tag{3}$$

where γ is the angle between the diffraction beam and the normal of the crystal surface. At point D the phase change Φ_D has the same form as Eq. (3) with γ replaced by $90^\circ - \gamma$. From the conditions of the total internal reflection at points B and D we obtain $\theta_c < \gamma < 90^\circ - \theta_c$, where θ_c is the critical angle. The diffraction beam from region E propagates a distance l_3 to reach region A.

The self-pumped phase conjugation counterpropagates with the incident pulses and undergoes refraction at the air–crystal interface again. The angular dispersion introduced by the refraction is

$$\frac{d\theta'}{d\lambda} = \frac{\sin\theta}{n\cos\theta}\left(\frac{dn}{d\lambda}\right), \tag{4}$$

where $n(\omega)\sin\alpha(\omega) = \sin\theta$.

The angular dispersion responsible for GVD is obtained by[6]

$$\begin{aligned}\frac{d^2\Psi_1}{d\Omega^2} = &-\frac{l_1\omega_l}{c}\left(\frac{d\alpha}{d\Omega}\right)^2 - \frac{l_2\omega_l}{c}\left(\frac{d\Theta}{d\Omega}\right)^2\\ &- \frac{(l_1+l_3)\omega_l}{c}\left(\frac{d\Theta}{d\Omega}\right)^2 - \frac{l_4\omega_l}{c}\left(\frac{d\theta'}{d\Omega}\right)^2\\ &+ \frac{d^2\Phi_B}{d\Omega^2} + \frac{d^2\Phi_D}{d\Omega^2},\end{aligned} \tag{5}$$

where l_4 is the distance between observation plane P and the crystal and

$$\begin{aligned}\frac{d^2\Phi_i}{d\Omega^2} = &-\tan\frac{\Phi_i}{2}\left(\frac{d\Phi_i}{d\Omega}\right)^2 + \frac{n^3\lambda^2}{2\pi c}\frac{\tan^2\gamma_i}{\tan^2\Phi_i}\\ &\times\left[\frac{\lambda^2}{2\pi c}\left(\frac{dn}{d\lambda}\right) + \frac{4}{3n^2\sin^2\gamma_i - 1}\right]\\ &\times\left(\frac{dn}{d\lambda}\right)\left(\frac{d\Phi_i}{d\Omega}\right)(i = B, D)\\ &-\frac{\lambda}{2\pi c}\left(\frac{d\Phi_i}{d\Omega}\right)\left(\lambda\frac{d^2n}{d\lambda^2} + 2\frac{dn}{d\lambda}\right)\Big/(dn/d\lambda),\end{aligned} \tag{6}$$

where

$$\gamma_i = \begin{cases}\gamma & i = B\\ 90^\circ - \gamma & i = D\end{cases}.$$

Inserting Eqs. (1)–(4) into Eq. (5), we obtain

$$\begin{aligned}\frac{d^2\Psi_1}{d\Omega^2} = &-\frac{4\lambda^3}{2\pi c^2}\left[\frac{l_1\sin^2\theta}{n^2(n^2 - \sin^2\theta)}\left(\frac{dn}{d\lambda}\right)^2\right.\\ &+\frac{(l_1+l_2+l_3)}{(2\Lambda n)^2 - \lambda^2}\left(1 - \frac{\lambda}{n}\frac{dn}{d\lambda}\right)^2\\ &\left.+\frac{l_4\sin^2\theta}{n^2\cos^2\theta}\left(\frac{dn}{d\lambda}\right)^2\right] + \frac{d^2\Phi_B}{d\Omega^2} + \frac{d^2\Phi_D}{d\Omega^2}.\end{aligned} \tag{7}$$

The last two terms on the right-hand side of Eq. (7) are 5 orders of magnitude smaller than the first term.

The beam propagates inside the crystal, which also contributes to the dispersion. Let the cumulative mean path be L; then the additional second-order dispersion parameter is[6]

$$\frac{d^2\Psi_2}{d\lambda^2} = \frac{d^2}{d\Omega^2}\left(\frac{\Omega}{c}nL\right) = \frac{\lambda^3}{2\pi c^2}L\frac{d^2n}{d\lambda^2}. \tag{8}$$

The total dispersion responsible for GVD is

$$\frac{d^2\Psi}{d\Omega^2} = \frac{d^2\Psi_1}{d\Omega^2} + \frac{d^2\Psi_2}{d\Omega^2}. \tag{9}$$

If we assume that the absorption of the crystal is negligible, the self-pumped phase-conjugate field is given by[6]

$$E_{out}(\Omega) = R(\Omega)\exp[-i\Psi(\Omega)]E(\Omega), \tag{10}$$

where $E(\Omega)$ is the incident field's spectrum.

We assume that $R(\Omega)$ does not change over the pulse spectrum, whereas $\Psi(\Omega)$ does. We consider an unchirped incident Gaussian pulse, e.g., $E(\Omega, 0) = A_0\exp[-i(\tau_{G0}/2)^2\Omega^2]$ and the expansion of $\Psi(\Omega)$ to the second order. Then the time-dependent self-pumped phase-conjugate electric field that we obtain by Fourier transforming Eq. (10) can be written as

$$\begin{aligned}E_{out}(t, L) = A_1\exp\Bigg(&-\left[1 - i\frac{b_2}{(\tau_{G0}/2)^2}\right]\\ &\times\left\{\frac{(t+b_1)}{\tau_{G0}[1 + b_2^2/(\tau_{G0}/2)^4]^{1/2}}\right\}^2\Bigg),\end{aligned} \tag{11}$$

where A_1 is a complex constant, $b_2 = d^2\Psi_1/d\Omega^2 + \beta_2 L/2$, and $\beta_2 = \lambda^3/2\pi c^2(d^2n/d\lambda^2)$, which can be determined from the Sellmeier equation.[8] The expansion coefficients of $\Psi(\Omega)b_0$, b_1 have no effect on the pulse; b_2 produces a quadratic spectral phase. The pulse duration is given by

$$\tau_G(L) = \tau_{G0}[1 + b_2^2/(\tau_{G0}/2)^4]^{1/2}. \tag{12}$$

Figure 2 shows simulations of the twofold derivation of the dispersion as a function of wavelength. The parameters are $\theta = 45^\circ$, $l_1 = 2$ mm, $l_1 + l_2 + l_3 = 8$ mm, $l_4 = 140$ mm, and $L = 5.0$ mm, which are chosen to mimic the experimental conditions. The solid curve represents the dispersion when the angular dispersions are not considered. The dashed, dotted, and dashed–dotted curves are the total dispersion with grating spacings of 1.0, 0.5, and 0.3 μm, respectively. We note that the angular dispersion always results in negative GVD, which compensates for the positive GVD that is due to the propagation of the finite crystal path. Figure 3 shows the widths of the transmitted and the phase-conjugate pulses as functions of wavelength. For $\Lambda = 1.0$ and $\Lambda = 0.5$ μm the self-pumped phase conjugate-pulse is much narrower than the transmitted pulse in a wide wavelength region. By managing the angular dispersion of the dynamic gratings, for example by changing the orientation of the crystal, we can control the total dispersion

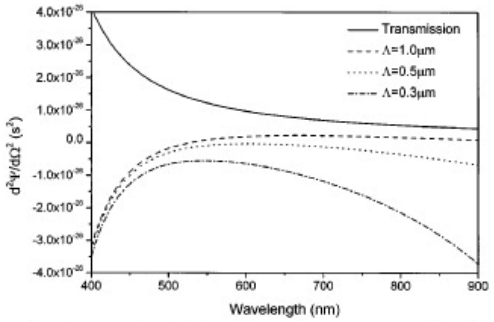

Fig. 2. Second derivative of the dispersion as a function of wavelength. Solid curve, dispersion with angular dispersion not considered. For the other curves, for the total dispersion including the angular dispersions, the transmission grating spacings Λ are shown.

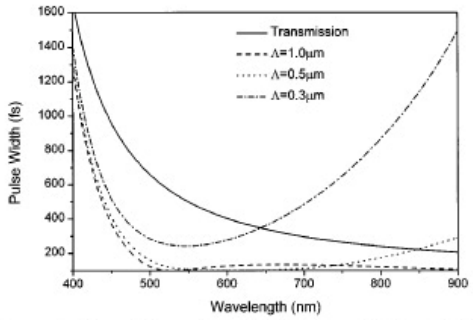

Fig. 3. Pulse width as a function of wavelength. Solid curve, width of the transmitted pulse with angular dispersions not considered. For the other curves, which represent the widths of the self-pumped phase-conjugate pulses, the transmission grating spacings Λ are shown.

of the phase conjugator and then the width of the self-pumped phase-conjugate pulse. A time lens effect can be achieved with the self-pumped phase conjugator.[9]

In the above analysis we consider only the beam that propagates along *OABDEAO*. It is possible that the beam propagates along *OAEDBAO*. Then the angular dispersion can be given by

$$\frac{d^2\Psi_1'}{d\Omega^2} = -\frac{4\lambda^3}{2\pi c^2}\left[\frac{(l_1+l_3)\sin^2\theta}{n^2(n^2-\sin^2\theta)}\left(\frac{dn}{d\lambda}\right)^2 + \frac{(l_1+l_2)}{(2\Lambda n)^2-\lambda^2}\left(1-\frac{\lambda}{n}\frac{dn}{d\lambda}\right)^2 + \frac{l_4\sin^2\theta}{n^2\cos^2\theta}\left(\frac{dn}{d\lambda}\right)^2\right] + \frac{d^2\Phi_B}{d\Omega^2} + \frac{d^2\Phi_D}{d\Omega^2}. \quad (13)$$

We obtain similar simulation results with Figs. 2 and 3 by use of Eq. (13) instead of Eq. (7).

A cat mirror may consist simply of a single interaction region diffracting light to the corner for corner-cube reflection. The two regions A and E in Fig. 1 should shrink to one interaction region. In this case the dispersion has the same form as Eqs. (7) and (13). However, the distance l_3 should be the interaction region (grating) thickness.

We measure the widths of the phase-conjugate pulse and the transmitted pulse by use of an undistorted pulse with a duration of 100 fs.[7] The incident pulse (λ = 450 nm) is Fourier limited. The $BaTiO_3$ crystal is 0° cut, with dimensions of 4.56 mm × 6.75 mm × 5.69 mm. The self-pumped phase conjugation is generated along the 5.69-mm side. The incident angle is 45°. The autocorrelation of the incident pulse has a width of 156 fs. The cross correlations of the incident pulse with the phase-conjugate pulse and with the transmitted pulse have widths of 480 and 880 fs, respectively. The width of the phase-conjugate pulse (~300 fs) is narrower than that of the transmitted pulse (~600 fs). The relationship of the pulse duration to the incident angle is currently under investigation.

In conclusion, we have analyzed theoretically the dispersion of a femtosecond self-pumped phase conjugator in a cat mirror configuration. The negative angular dispersion of the refraction at the air–crystal interface and the dynamic gratings in the crystal compensate for the positive dispersion of the finite crystal path. We suggest that the total dispersion of the phase conjugator can be controlled by management of the angular dispersion of the gratings inside the crystal. When this compensation is complete the self-pumped phase-conjugate pulse can maintain the same width as the incident pulse, as was observed at 797 nm by Yau *et al.*[1,2] Our experiment has qualitatively proved the theoretical predictions.

I thank K. Minoshima, K. Seta, and H. Matsumoto of the National Research Laboratory of Metrology, Tsukuba, Japan, for stimulating discussions. Some of the experiments were carried out at that laboratory. My e-mail address is changxi@hotmail.com.

References

1. H.-F. Yau, P.-J. Wang, E.-Y. Pan, J. Chen, and J. Y. Chang, Opt. Commun. **135,** 331 (1997).
2. H.-F. Yau, P.-J. Wang, E.-Y. Pan, and J. Chen, Opt. Lett. **21,** 1168 (1996).
3. A. Yariv, D. Fekete, and D. M. Pepper, Opt. Lett. **4,** 52 (1979).
4. J. Feinberg, Opt. Lett. **7,** 486 (1982).
5. G. P. Agrawal, *Nonlinear Fiber Optics* (Academic, San Diego, Calif., 1989), Chaps. 2 and 3.
6. J.-C. Diels and W. Rudolph, *Ultrashort Laser Pulse Phenomena: Fundamentals, Techniques, and Applications on a Femtosecond Time Scale* (Academic, San Diego, Calif., 1995), Chap. 2.
7. R. M. Brubaker, Y. Ding, D. D. Nolte, M. R. Melloch, and A. M. Weiner, IEEE J. Quantum Electron. **33,** 2150 (1997).
8. K. Buse, S. Riehemann, S. Loheide, H. Hesse, F. Mersch, and E. Kratzig, Phys. Status Solidi A **135,** K87 (1993).
9. B. H. Kolner and M. Nazarathy, Opt. Lett. **14,** 630 (1989).

N. Nayak

Effect of Dissipative Forces on the Theory of a Single-Atom Microlaser

S.N. Bose National Centre for Basic Sciences, Salt Lake City, Calcutta, India

A single-atom microlaser involving Poissonian input of atoms with a fixed f light time through an optical resonator is described. The influence of the cavity reservoir during the interactions of successive individual atoms with the cavity field is included in the analysis. Atomic decay is also considered, as it is nonnegligible in the optical regime. During the random intervals of absence of any atom in the cavity, the field evolves under its own dynamics. The steady-state characteristics of the cavity field are discussed. Away from laser threshold, the field can be nonclassical in nature.

***Keywords*: Microlaser, Single-atom laser, Dissipative forces**

The single-atom laser, an optical counterpart of the micromaser, has generated extensive interest after the recent experimental demonstration by An *et al.*[1] In that experiment, two-level ^{138}Ba atoms in their upper states were pumped into an optical cavity in such a way that the average number of atoms in the resonating mode satisfied the condition $\langle N \rangle \leq 1.0$. The average number of photons $\langle n \rangle$ in the mode showed a linear dependence on the pump until $\langle N \rangle = 0.6$. But a further increase in $\langle N \rangle$ resulted in a thresholdlike jump in $\langle n \rangle$. Calculations based on a single-atom theory, such as the one given in Ref. 1, can explain the linear regime only. An and Feld[2] incorporated the cavity-mode structure into the single-atom theory to explain this jump. Kolobov and Haake[3] addressed the problem by use of a Poissonian pumping model with partial overlaps of the travel times of successive atoms in the cavity. Alternative explanations[4,5] have also been proposed to explain the thresholdlike structure.

In this Letter a slightly different pump mechanism in the microlaser setup is addressed: Atoms are streamed into the cavity in such a way that strictly one atom can pass through it at a time. The pumping is Poissonian, with the intervals between successive atomic flights being random. Thus the flight time through the cavity is fixed for each atom. In other words, an exact optical counterpart of a micromaser setup[6] is considered here. The single-atom laser theories available in the literature, for example, in Ref. 7, involve analysis of the steady-state properties of the Jaynes–Cummings interaction[8] in a damped cavity.[9] The single-atom theory of Filipowicz *et al.*[10] needs recasting because it does not consider atomic damping, which is important in the optical regime, and because of the cavity-enhancement factor, the so-called Purcell factor. In addition, the theory disregards leakage of radiation from the cavity during the atom–field interaction. The magnitudes of the cavity dissipation constant and the atom–field coupling constant in the microlaser experiment[1] indicate that radiation dissipation from the optical resonator is nonnegligible during the entire dynamics, irrespective of the presence of any atom in the cavity.

The above factors lead us to the need for a theory capable of handling reservoir-induced interactions and the Jaynes–Cummings interactions[8] simultaneously. The theory that I proposed in Ref. 11 may be suitable for the present purpose. The theory assumes that the atom–field coupling constant is independent of cavity-mode structure, which is all right for the microwave cavity.[6] In fact, such a situation is necessary for the generation of nonclassical fields.[4] In the optical cavity described in Ref. 1, atoms travel through a length of ~40 wavelengths of the interacting mode, thus making the coupling constant dependent on the mode structure. However, a novel and simple technique for streaming the atoms through the cavity, adopted by An *et al.*[12] to improve their earlier setup,[1] provides a uniform atom–field coupling constant in the cavity. This setup with single-atom events would be suitable for generating nonclassical fields in the optical regime. With such a system in mind, we follow the method in Ref. 11.

We assume that atoms arrive individually at the cavity, with an average interval $\bar{t}_c = 1/R$, where R is the flux rate of atoms. We have $t_c = \tau + t_{\rm cav}$, where τ is the interaction time, fixed for every atom, and $t_{\rm cav}$ is the random time lapse between one atom leaving and a successive atom entering the cavity. $\bar{t}_c$ is the average of t_c taken over a Poissonian distribution in time of incoming atoms. The cavity field evolves from a near vacuum by means of this repetitive dynamics, as thermal photons in the optical cavity are almost nonexistent. Thus, during τ, we have to solve the equation of motion:

$$\dot{\rho} = -i[H,\rho] - \kappa(a^\dagger a\rho - 2a\rho a^\dagger + \rho a^\dagger a) - \gamma(S^+S^-\rho - 2S^-\rho S^+ + \rho S^+S^-), \qquad (1)$$

where H is the Jaynes–Cummings Hamiltonian[8] and κ and γ are the cavity-mode and the atomic-decay constants, respectively. a is the photon annihilation operator, and S^+ and S^- are the Pauli pseudospin operators for the two-level atomic system. During $t_{\rm cav}$, the cavity field evolves under its own dynamics, represented by Eq. (1), with $H = \gamma = 0$. The method for obtaining a coarse-grained time derivative, which is valid for a Poissonian process,[13,14] is given in detail

in Ref. 11 for the photon-number distribution $P_n = \langle n|\rho|n\rangle$. The steady-state photon statistics is then

$$P_n = P_0 \prod_{m=1}^{n} v_m , \tag{2}$$

and P_0 is obtained from the normalization $\sum_{n=0}^{\infty} P_n = 1$. The v_n is given by the continued fractions

$$v_n = f_3^{(n)}/[f_2^{(n)} + f_1^{(n)} v_{n+1}], \tag{3}$$

with $f_1^{(n)} = (Z_n + A_{n+1})/\kappa$, $f_2^{(n)} = -2N + (Y_n - A_n)/\kappa$ and $f_3^{(n)} = -X_n/\kappa$. $N = R/2\kappa$ is the number of atoms passing through the cavity in a photon lifetime. $A_n = 2n\kappa$, and X_n, Y_n, and Z_n are given by

$$X_n = R \sin^2(g\sqrt{n}\tau)\exp\{-[\gamma + (2n-1)\kappa]\tau\},$$

$$\begin{aligned} Y_n = \frac{1}{2} R\Bigg(& \left[2\cos^2(g\sqrt{n+1}\,\tau) - \frac{1}{2}(\gamma/\kappa + 2n + 1) \right. \\ & \left. + F_1(n-1) \right] \exp\{-[\gamma + (2n+1)\kappa]\tau\} \\ & + \left[\frac{1}{2}(\gamma/\kappa + 2n + 1) - F_2(n-1) \right] \\ & \times \exp\{-[\gamma + (2n-1)\kappa]\tau\} \Bigg), \end{aligned}$$

$$\begin{aligned} Z_n = \frac{1}{2} R\Bigg(& \left[\frac{1}{2}(\gamma/\kappa + 2n + 3) + F_2(n) \right] \\ & \times \exp\{-[\gamma + (2n+1)\kappa]\tau\} \\ & - \left[\frac{1}{2}(\gamma/\kappa + 2n + 3) + F_1(n) \right] \\ & \times \exp\{-[\gamma + (2n+3)\kappa]\tau\} \Bigg). \end{aligned}$$

The functions F_1 and F_2 are

$$\begin{aligned} F_i(n) = & \frac{\kappa/4g}{(\sqrt{n+2} - \sqrt{n+1})^2} \Bigg(\frac{\gamma}{\kappa}(\sqrt{n+2} - \sqrt{n+1}) \\ & \times \sin(2g\sqrt{m}\,\tau) - \frac{\gamma}{g}\cos(2g\sqrt{m}\,\tau) \\ & - \{2n + 3 + 2[(n+1)(n+2)]^{1/2}\} \\ & \times (\sqrt{n+2} - \sqrt{n+1})\sin(2g\sqrt{m}\,\tau) \Bigg) \\ & + \frac{\kappa/4g}{(\sqrt{n+2} + \sqrt{n+1})^2} \\ & \times \Bigg(\pm \frac{\gamma}{\kappa}(\sqrt{n+2} + \sqrt{n+1}) \\ & \times \sin(2g\sqrt{m}\,\tau) - \frac{\gamma}{g}\cos(2g\sqrt{m}\,\tau) \\ & \mp \{2n + 3 - 2[(n+1)(n+2)]^{1/2}\} \\ & \times (\sqrt{n+2} + \sqrt{n+1})\sin(2g\sqrt{m}\,\tau) \Bigg), \end{aligned}$$

where $m = n + 2$ and $n + 1$ for $i = 1$, and $i = 2$, respectively, with the upper sign for $i = 1$. Once P_n is obtained, we can describe the characteristics of the cavity field by evaluating its various moments.

We find that the photon statistics of the cavity field given by Eqs. (2) and (3) is a function of the dimensionless parameters N, κ/g, and γ/g. The theory in Ref. 10 does not take into account atomic relaxation. As cavity dissipation during τ is neglected, the photon distribution function derived in Ref. 10 is dependent on κ only through the parameter $N = R/2\kappa$. Hence, in the context of the microlaser, it is difficult to make a proper judgment of the dissipative effects on the photon statistics based on the work of Filipowicz *et al.*[10] Reference 11 discusses in detail the degree of influence of the reservoir-induced interactions on the steady-state photon statistics. That study indicates that the influence of the interactions is nonnegligible for the optical cavities of the type used in the studies reported in Refs. 1 and 12. In fact, it is found that the photon statistics obtained by use of the results from Ref. 10 (dashed–dotted curves in Figs. 1 and 2) mostly differ from the present results. The pump parameter $D = \sqrt{N}\,g\tau$ is introduced here, as I find it useful for the description of microlaser characteristics. The structures in $\langle n\rangle$ as D is varied for fixed N (see Fig. 1) reflect the characteristics of the Jaynes–Cummings interaction.[8] Soon after the threshold is attained at $D = \sim 1.0$, the photon number rises sharply. The reason is as follows: The field is almost in vacuum before the first atom enters the cavity. Thus the atoms that are initially in their upper states contribute varying fractions of their energies to the cavity, and at $n = N$ and $D = \pi/2$ the atoms are completely in their respective lower states. Thus $\langle n\rangle$ peaks at $D = \sim 1.6$, depending on κ, γ, and N. For higher κ and γ, the peak moves slightly toward higher D because the threshold is attained at higher D. This happens even for increasing R, which is due to an increase in the percentage of time $R\tau \times 100\%$ in the duration of 1 s taken by R atoms in interacting with the cavity field, resulting in an increase in dissipation of energy to the atomic reservoir. It is further found that $\langle n\rangle = 0$ near $D = 31.4, 62.8, 94.2, \ldots$, which gives $g\tau = \pi, 2\pi, 3\pi, \ldots$, respectively. At such values of $g\tau$, the atom absorbs

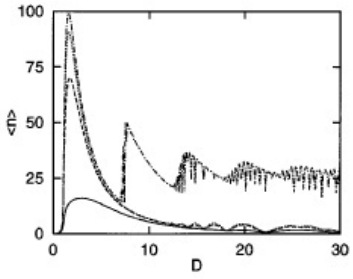

Fig. 1. Cavity field intensity, proportional to $\langle n\rangle$, as a function of the pump parameter D for $N = 100$ and $\gamma/g = 0.1$. Solid curve, $\kappa/g = 0.01$; dashed curve, $\kappa/g = 0.001$; dotted curve, $\kappa/g = 0.0001$; dotted–dashed curve, results from Ref. 10, in which $\kappa = \gamma = 0.0$ during τ.

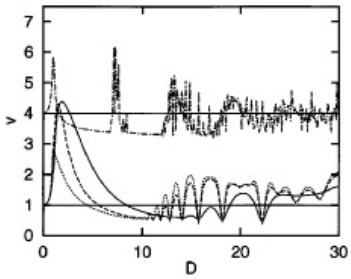

Fig. 2. Variance of the cavity field, v, versus pump parameter D. The other parameters are the same as in Fig. 1. For clarity, the dashed–dotted curve is shifted upward by 3.0. The horizontal lines are $v = 1.0, 4.0$. The sub-Poissonian nature of the radiation field is indicated by $v < 1.0$.

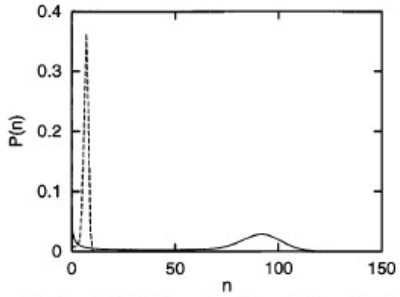

Fig. 3. Photon distribution function $P(n) = P_n$ for $N = 100$, $\gamma/g = 0.1$, and $\kappa/g = 0.001$. Solid curve, $D = 1.7$; dashed curve, $D = 10.0$.

the photon that it has emitted before leaving the cavity.

Figure 2 shows that the variance of the cavity field, $v = [(\langle n^2\rangle - \langle n\rangle^2)/\langle n\rangle]^{1/2}$, increases sharply at $D = \sim 1.6$, where $\langle n\rangle$ also peaks (see Fig. 1). It is found that near this value of D the P_n is doubly peaked at $n = 0$ and $n \simeq N$, as shown in Fig. 3, and this increases the variance in photon number. However, for a slightly higher value of D the cavity field is highly sub-Poissonian in nature (Figs. 2 and 3). This is also the case for still-higher values of D. The sub-Poissonian nature of the cavity field appears because the flight time τ is short compared with the atomic lifetime $(2\gamma)^{-1}$ as well as the photon lifetime $(2\kappa)^{-1}$, as was discussed in detail in Ref. 11. Such situations, which are depicted in Fig. 2, do not happen in conventional lasers. Thus it is found that the photon field characteristics in the present microlaser case (Figs. 2 and 3) are different from those of a conventional laser.[15] Further, it may be noted in Fig. 1 that $\langle n\rangle$ gets very small as D is increased, because the increase in interaction time τ increases the influence of atomic as well as cavity reservoirs on the atom–field interaction. The sub-Poissonian nature of the cavity field appears for such values of D since the situation $\tau < (2\tau)^{-1}, (2\kappa)^{-1}$ is met in the range of D depicted in Figs. 1 and 2.

The cavity field intensity, which is proportional to $\langle n\rangle$, saturates as N is increased for fixed τ. The saturation value of $\langle n\rangle$ depends on τ, as dictated by the Jaynes–Cummings interactions.[8] This saturation characteristic is not seen in Fig. 1, in which the increase in D is due to an increase in τ for fixed N.

The characteristics of a single-atom microlaser capable of generating nonclassical optical fields in the realistic regimes of atomic and cavity dissipations (e.g., $\kappa/g = 0.01$ and $\gamma/g = 0.1$) have been analyzed. Results have also been displayed for $\kappa/g = 0.001, 0.0001$ in the figures. This shows the influence of κ on the photon statistics that can be attained if the cavity Q factor in the present experimental setup is enhanced by a factor of 100 or more. In addition, the influences of atomic as well as field reservoirs on the coherent atom–field interaction have been included. Poissonian pumping of atoms into the cavity, which was the case in previous experiments,[1,12] was considered. However, the parameter N in the present study has to be distinguished from $\langle N\rangle$ in those experiments, in which the statistical averaging was taken over $N_0 = 1, 2, 3, \ldots$ atomic events. The arrival of N_0 atoms at the cavity is, however, Poissonian. Yang and An,[4] in their attempt to analyze the experimental results presented in Ref. 1, considered values as great as $N_0 = 15$, whereas here N was just a simple addition of single-atom events in the photon lifetime $(2\kappa)^{-1}$. The technique adopted in Ref. 12 can already be used to select atoms with a particular velocity. Further refinement to restrict the dynamics to only $N_0 = 1$ events should be possible. Then it would be possible to have nonclassical optical fields of the type shown in Fig. 2.

I thank G. S. Agarwal for suggesting the problem studied in this work.

References

1. K. An, J. J. Childs, R. R. Dasari, and M. S. Feld, Phys. Rev. Lett. **73,** 3375 (1994).
2. K. An and M. S. Feld, Phys. Rev. A **52,** 1691 (1995).
3. M. I. Kolobov and F. Haake, Phys. Rev. A **55,** 3033 (1997).
4. C. Yang and K. An, Phys. Rev. A **55,** 4492 (1997).
5. K. An and M. S. Feld, Phys. Rev. A **56,** 1662 (1997).
6. G. Rempe, F. Schmidt-Kaler, and H. Walther, Phys. Rev. Lett. **64,** 2783 (1990).
7. C. Ginzel, H. Briegel, U. Martini, B. Englert, and A. Schenzle, Phys. Rev. A **48,** 732 (1993).
8. E. T. Jaynes and F. W. Cummings, Proc. IEEE **51,** 89 (1963).
9. G. S. Agarwal and S. Datta Gupta, Phys. Rev. A **42,** 1737 (1990).
10. P. Filipowicz, J. Javanainen, and P. Meystre, Phys. Rev. A **34,** 3077 (1986); P. Meystre, G. Rempe, and H. Walther, Opt. Lett. **13,** 1078 (1988).
11. N. Nayak, Opt. Commun. **118,** 114 (1995).
12. K. An, R. R. Dasaari, and M. S. Feld, Opt. Lett. **22,** 1500 (1997).
13. J. Bergou, L. Davidovich, M. Orszag, C. Benkert, M. Hillary, and M. O. Scully, Phys. Rev. A **40,** 5073 (1989).
14. L. Davidovich, S.-Y. Zhu, A. Z. Khoury, and C. Su, Phys. Rev. A **46,** 1630 (1992).
15. See, e.g., M. Sargent III, M. O. Scully, and W. E. Lamb, Jr., *Laser Physics* (Addison-Wesley, Reading, Mass., 1974).

O. Dühr
E.T.J. Nibbering
G. Korn
G. Tempea
F. Krausz

Max-Born-Institut für Nichtlineare Optik und Kurzzeitspektroskopie, Berlin, Germany

Generation of Intense 8-fs Pulses at 400 nm

Frequency-doubled pulses from a sub-40-fs, 1-kHz Ti:sapphire amplifier system are spectrally broadened in an argon-filled hollow waveguide. Compression of the self-phase-modulated pulses is implemented with chirped mirrors and a prism pair, yielding 8-fs, 15-mJ pulses in the violet spectral range.

Keywords: **Ti:S laser, Femtosecond pulses, Wavelength conversion**

Optical pulse compression has been established as a powerful technique for generating intense sub-10-fs pulses in the red and near-infrared spectral range. Self-phase modulation (SPM) in a single-mode fiber followed by propagation through a dispersive delay line consisting of prisms and diffraction gratings was successfully exploited more than a decade ago for production of 6-fs, 1-nJ, 8-kHz pulses at 620 nm.[1] Recently, further pulse shortening was achieved at higher repetion rates and (or) higher pulse energies. Pulses near 800 nm at a 1-MHz repetition rate with durations as short as 4.5 fs and energies up to 6 nJ were obtained by use of a cavity-dumped Ti:sapphire oscillator and an improved dispersive delay line incorporating chirped mirrors and a prism pair.[2] Replacement of the single-mode fiber with a gas-filled hollow waveguide allowed scaling to much higher pulse energies.[3] SPM in a gas-filled hollow fiber followed by dispersive compression in ultrabroadband chirped dielectric mirrors yielded 4.5–5-fs submillijoule pulses with peak powers up to 0.1 TW at a 1-kHz repetition rate.[4,5]

The generation of intense sub-10-fs pulses was recently extended into the 500–700-nm wavelength range by use of a continuum-seeded noncollinear optical parametric amplifier pumped by the second harmonic of a Ti:sapphire laser.[6,7] To our knowledge, these are the shortest wavelengths at which powerful sub-10-fs light pulses had been produced. In the violet–ultraviolet range microjoule-energy pulses of ~20 fs in duration were demonstrated recently.[8–10] In this Letter we report the generation of 15-μJ, 8-fs pulses at a wavelength of approximately 400 nm.

This experiment draws on our previous work, which resulted in the production of powerful 20-fs pulses tunable from 360 to 440 nm by use of a hollow-waveguide quartz-prism compressor seeded with the frequency-doubled output of a 1-kHz femtosecond Ti:sapphire amplifier system.[10] Pulse shortening was found to be limited by a residual third-order spectral phase left uncompensated in the compressor stage. This system has been improved in several respects. First, shorter frequency-doubled seed pulses with a duration of 29 fs are used. Second, SPM is carefully optimized in the hollow waveguide. Last but not least, the quartz-prism compressor is supplemented with specially designed chirped mirrors that allow reduction of undesirable third-order dispersion (TOD) in the compression system.

Powerful ultrashort pulses at 800 nm are generated with a home-built Ti:sapphire laser system that utilizes chirped-pulse amplification.[11] The seed pulses, as generated by a 15-fs chirped-mirror-compensated Ti:sapphire oscillator,[12] are stretched by a factor of 10,000 in an all-reflective pulse stretcher[13] capable of controlling higher-order dispersion. A lamp-pumped Q-switched intracavity-frequency-doubled Nd:YLF laser delivering an average output power of 23 W at 532 nm pumps a 10-round-trip regenerative Ti:sapphire amplifier and a two-pass Ti:sapphire power amplifier at a repetition rate of 1 kHz. The 2.4-mJ amplified pulses, with a spectrum peaking at 800 nm, are recompressed with a 50%-transmitting reflective grating pair to a pulse duration of 38 fs.

Efficient frequency doubling of downcollimated 1-mJ 38-fs fundamental pulses is achieved in 100-μm-thick β-barium borate (BBO), resulting in violet pulses with energies up to 400 μJ and a spectral width of 8 nm [see Fig. 1(a)]. Changing the distance of the compressor gratings in the amplifier system slightly introduces a small negative chirp in the fundamental that precompensates for dispersion in the doubling crystal and allows us to achieve high conversion efficiencies, up to 40%. Self-diffraction (SD) third-order autocorrelation measurements of the violet pulses in a 100-μm-thick potassium dihydrogen phosphate (KDP)

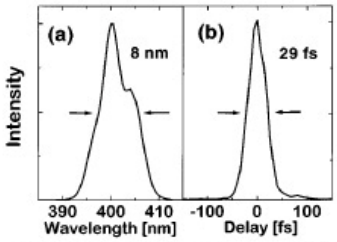

Fig. 1. (a) Spectrum and (b) SD autocorrelation trace of the output of the BBO crystal. A correlation width of 39 fs corresponds to a pulse width of 29 fs.

crystal [Fig. 1(b)] reveal a significantly shorter pulse duration [29 fs (FWHM)] for the second harmonic than for the fundamental.

For spectral broadening, violet pulses of 300-μJ energy are focused with a concave mirror with radius $R = 1$ m into a hollow waveguide with a bore diameter of 220 μm and filled with argon at pressure $p = 0.4$–0.6 bars (1 bar = 10,000 Pa). The choice of argon as the nonlinear medium is a good compromise between a moderate ionization threshold and moderate nonlinearity, whereas in the case of helium or neon the ionization properties are better but the nonlinearity is much smaller. Even at these moderate gas pressures the intense light induces strong spectral broadening, as shown in Figs. 2 and 3. We estimate the calculated optimum fiber length L_{opt} for generating a spectrally broadened pulse with a nearly quadratic spectral phase (i.e., linear chirp in the time domain) to be 40 cm for $\lambda_0 = 400$ nm, using $L_{opt} = (6L_{nl}L_D)^{0.5}$,[14] where $L_{nl} = 1/\gamma P_0 = 1.3$ cm and $L_D = T_0^2/\beta_2 = 1.9$ m. Here $P_0 = 26$ GW is the peak power of the seed pulses, and $T_0 = 48$ fs is defined by $P(T_0) = P_0/e$. Further, $\gamma = n_2\omega_0/cA_{eff} = 3.01 \times 10^{-11}$ W^{-1}cm^{-1} is the nonlinear coefficient, $n_2 = 3.10 \times 10^{-19}$ cm^2 W^{-1} is the nonlinear refractive index at $p = 0.6$ bars,[15] A_{eff} is the effective cross-sectional area of the hollow waveguide, and $\beta_2 = 12.41$ fs^2 cm^{-1} is the group-velocity dispersion, including contributions from the waveguide and the argon gas.[16] To introduce some discrimination against higher-order transverse propagation modes, which may also be excited to some extent owing to incomplete matching of the free-propagating input beam to the fundamental EH_{11} mode of the waveguide, we use a 70-cm-long waveguide. The output pulse energy delivered in the fundamental mode amounts to approximately 80 μJ, implying a throughput of 26%. The low throughput is assigned to a low coupling efficiency owing to the elliptic beam profile of the second-harmonic pulse, preventing good mode matching to the EH_{11} mode simultaneously in both transverse directions.

The fiber output is collimated with a concave aluminum mirror with $R = 2$ m and reflected six times off chirped multilayer mirrors consisting of 42 alternating layers of SiO_2 and Ta_2O_5. The mirrors exhibit high reflectivity from 330 to 460 nm and are expected to introduce a nearly constant group-delay dispersion (GDD) of approximately -20 fs^2 from 350 to 430 nm. We show a theoretical estimate of the GDD and the TOD in Fig. 2. Employing these chirped mirrors with negligible TOD and minimizing the optical path length in the prisms allows us to reduce the prism apex distance of 45 cm, compared with 130 cm in our previous experiment.[10] Although the dispersion characteristics of the mirrors have still to be measured, we deduce from the shorter prism distance that the mirrors introduce the amount of GDD per bounce that was predicted. The exclusive use of chirped mirrors for pulse compression is currently prevented by the low dispersion and the high loss (10%) that they introduce per bounce. The origin of this anomalously high reflection loss under exposure to high peak intensities remains to be found.

Figure 3 summarizes the results of a SD frequency-resolved optical gating (FROG) measurement[17] of compressed pulses generated at an argon pressure of $p = 0.4$ bars. Figures 3(a) and 3(b) depict the spectrum and the measured SD correlation (filled circles) of the compressed pulses, respectively. The measured SD FROG trace is shown in Fig. 3(c). Figure 3(d) plots the retrieved intensity (solid curve) and phase (dashed curve) of the pulse, yielding a pulse duration (FWHM) of 13 fs and a small amount of residual phase at the pulse center.

The shortest pulse was generated by an increase in pressure of 0.6 bars, which led to further spectral broadening, as revealed by Fig. 4(a). A slight readjustment of the amount of glass introduced by the first prism proved necessary for optimum pulse compression. The SD trace of the compressed pulses [Fig. 4(b)] results in a third-order autocorrelation width of less than 11 fs. We recorded this trace with the stringent requirement of acquisition by use of only those pulses for which the energy and bandwidth fluctuations were less than $\pm 5\%$ of the average value. This excludes any erroneous broadening of the signals owing to intensity fluctuations of the seed pulse. Unfortunately, however, we have not yet implemented these stringent requirements in the acquisition of FROG traces. To determine the deconvolution factor

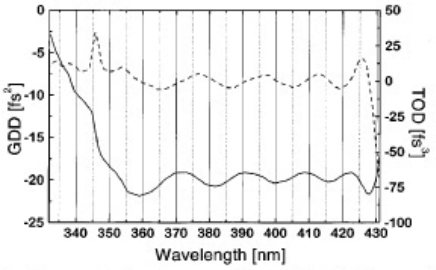

Fig. 2. Theoretical estimate of the GDD (solid curve) and the TOD (dashed curve) properties of the chirped mirrors.

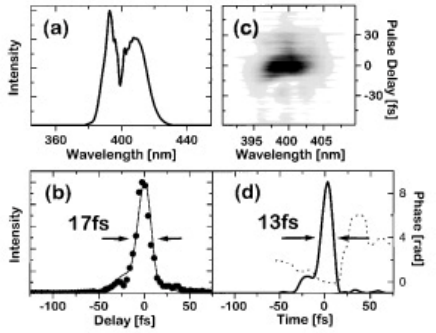

Fig. 3. (a) Spectrum, (b) SD autocorrelation, (c) SD FROG, and (d) retrieved pulse intensity and phase of compressed blue pulses obtained with 0.4-bar Ar in the hollow fiber. A calculated SD trace [solid curve in (b)] compares well with the experimental values (filled circles).

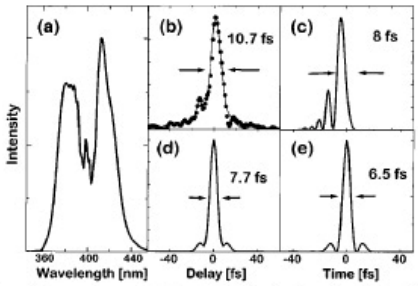

Fig. 4. SD autocorrelation [filled circles in (b)] of compressed blue pulses obtained with 0.6-bar Ar in the hollow fiber with the spectrum given in (a). The solid curves in (b) and (c) are the calculated SD signal- and pulse-intensity profiles, respectively, as described in the text. The Fourier-transform-limited SD signal and the temporal intensity profile are shown in (d) and (e), respectively.

and the residual higher-order phase, we can analyze the compressed pulses only by a fit of the spectral phase,

$$\Phi(\omega) = \Phi_0 + \frac{d\Phi}{d\omega}\bigg|_{\omega_0}(\omega - \omega_0) + \frac{1}{2}\frac{d^2\Phi}{d\omega^2}\bigg|_{\omega_0} \times (\omega - \omega_0)^2 + \frac{1}{6}\frac{d^3\Phi}{d\omega^3}\bigg|_{\omega_0}(\omega - \omega_0)^3 + \dots,$$

where the second- and third-order Taylor expansion coefficients are to be chosen to provide the best fit to the measured SD autocorrelation trace in Fig. 4(b). This fit is obtained with

$$\frac{d^2\Phi}{d\omega^2}\bigg|_{\omega_0} = 0\ \text{fs}^2, \qquad \frac{d^3\Phi}{d\omega^3}\bigg|_{\omega_0} = -70\ \text{fs}^3.$$

The corresponding pulse intensity envelope and the third-order autocorrelation trace are shown by the solid curves in Figs. 4(c) and 4(b), respectively. The small deviations between the experimental and the calculated traces may be due to higher-order phase terms. It is, however, clear that the remaining spectral cubic phase dominates the pulse characteristics. This analysis results in a pulse duration of 8 fs and a deconvolution factor of 1.35. These values are smaller than those obtained with second-harmonic autocorrelation because of the higher-order nonlinearity [$\chi^{(3)}$] that is responsible for self-diffraction. The pulse energy after compression is 15 μJ, giving rise to a peak power of approximately 2 GW. Owing to the diffraction-limited nature of the waveguide output, these pulses are expected to be focusable to intensities greater than 10^{16} W/cm^2 with $f/3$ optics.

The intensity envelope and the corresponding SD autocorrelation trace of a transform-limited signal with the spectrum shown in Fig. 4(a) are depicted in Figs. 4(e) and 4(d), respectively. The presence of small satellites relates to the modulated structure of the spectrum. Comparison of Figs. 4(c) and 4(e) implies that the compressed 8-fs violet pulses are 1.25 times Fourier limited.

We have demonstrated the generation of sub-10-fs gigawatt peak-power pulses in the violet spectral range for what we believe to be the first time. The performance of the system is currently limited by the loss and dispersion characteristics of the available chirped mirrors, which have been used in this wavelength range for what is to our knowledge the first time. The hollow-waveguide technique employed for SPM is not restricted to the pulse energies and spectral bandwidths demonstrated in this Letter. In fact, we recently achieved spectral broadening to bandwidths in excess of 70 nm near 400 nm with this same setup. Hence progress in short-wavelength chirped-mirror technology holds promise for the generation of intense 5-fs-scale light pulses in the violet–blue spectral range.

The authors are grateful to K. Ferencz of the Research Institute for Solid State Physics in Budapest for manufacturing the chirped mirrors and A. Nazarkin of the Max-Born-Institut in Berlin for helpful discussions. This research was partly supported by Austrian Science Fund grant Y44-PHY.

References

1. R. L. Fork, C. H. Brito Cruz, P. C. Becker, and C. V. Shank, Opt. Lett. **12,** 483 (1987).
2. A. Baltuška, Z. Wei, M. S. Pshenichnikov, and D. A. Wiersma, Opt. Lett. **22,** 102 (1997).
3. M. Nisoli, S. De Silvestri, and O. Svelto, Appl. Phys. Lett. **68,** 2793 (1996).
4. M. Nisoli, S. De Silvestri, O. Svelto, R. Szipöcs, K. Ferencz, C. Spielmann, S. Sartania, and F. Krausz, Opt. Lett. **22,** 522 (1997).
5. S. Sartania, Z. Cheng, M. Lenzner, G. Tempea, Ch. Spielmann, F. Krausz, and K. Ferencz, Opt. Lett. **22,** 1562 (1997).
6. G. Cerullo, M. Nisoli, and S. De Silvestri, Appl. Phys. Lett. **71,** 3616 (1997).
7. A. Shirakawa, I. Sakawe, and T. Kobayashi, in *Conference on Lasers and Electro-Optics*, Vol. 6 of 1998 OSA Technical Digest Series (Optical Society of America, Washington, D.C., 1998), postdeadline paper CPD11.
8. S. Backus, J. Peatross, M. M. Murnane, and H. C. Kapteyn, Opt. Lett. **21,** 665 (1996).
9. C. G. Durfee III, S. Backus, M. M. Murnane, and H. C. Kapteyn, Opt. Lett. **22,** 1565 (1997).
10. E. T. J. Nibbering, O. Dühr, and G. Korn, Opt. Lett. **22,** 1335 (1997).
11. D. Strickland and G. Mourou, Opt. Commun. **56,** 219 (1985).
12. A. Stingl, M. Lenzner, Ch. Spielmann, F. Krausz, and R. Szipöcs, Opt. Lett. **20,** 602 (1995).
13. B. E. Lemoff and C. P. J. Barty, Opt. Lett. **18,** 1651 (1993).
14. W. J. Tomlinson, R. H. Stolen, and C. V. Shank, J. Opt. Soc. Am. B **1,** 139 (1984).
15. H. J. Lehmeier, W. Leupacher, and A. Penzkofer, Opt. Commun. **56,** 67 (1985).
16. A. Dalgarno and A. E. Kingston, Proc. R. Soc. London Ser. A **259,** 424 (1966).
17. R. Trebino, K. W. DeLong, D. N. Fittinghoff, J. N. Sweetser, M. A. Krumbügel, B. A. Richman, and D. J. Kane, Rev. Sci. Instrum. **68,** 3277 (1997).

P.S. Banks
M.D. Feit
M.D. Perry

Laser Program,
Lawrence Livermore
National Laboratory,
California, U.S.A

High-Intensity Third-Harmonic Generation in Beta Barium Borate Through Second-Order and Third-Order Susceptibilities

The azimuthal dependence of third-order and cascaded second-order nonlinear coupling was used to measure the relative contributions of each to direct third-harmonic generation in b-barium borate. This permitted the measurement of the values of tensor elements $\chi^{(3)}_{10}$, $\chi^{(3)}_{11}$ ***and*** $\chi^{(3)}_{16}$ ***relative to the known*** $\chi^{(2)}_{ij}$. ***Finally, conversion efficiencies to 3ω of up to 6% were achieved with a femtosecond chirped-pulse amplification laser with 200 GW/cm^2 in collimated beams.***

Keywords: **Harmonic generation, Nonlinear coupling, Chirped pulses**

Third-harmonic generation (THG) in a single process is an idea that has been around since the inception of nonlinear optics.[1–3] However, since the process $\omega + \omega + \omega \rightarrow 3\omega$ is governed by the third-order nonlinear electric susceptibility $\chi^{(3)}$, the efficiency of such an interaction has been very low. To date, the high intensities needed to drive this process have confined most research to highly focused beams in gases or liquids. In fact, THG has come to refer mainly to the process of generating the second harmonic in one crystal followed by mixing the 2ω light with the remaining fundamental in a second phase-matched crystal. The advent of chirped-pulse amplification of femtosecond pulses has made it possible to achieve very high irradiances (>100 GW/cm^2) in collimated beams. This advance, combined with the change in damage mechanism for dielectrics below approximately 10 ps,[4] may make it possible to operate nonlinear crystals at the high intensity necessary to drive efficient THG while remaining safely below the damage threshold. This method presents the possibility of creating the third harmonic directly by use of a single nonlinear crystal rather than by the typical approach of second-harmonic generation (SHG) in one crystal followed by sum-frequency generation (SFG) in a second.

Some THG experiments have been done in solids, particularly calcite[5] and β-barium borate (BBO),[6,7] using focused, mode-locked pulses, but conversion efficiencies were limited to less than 1%. In addition to interaction through the third-order susceptibility, it has been suggested that non-phase-matched second-order processes can contribute significantly to THG,[6,8,9] similar to the use of cascaded second-order processes' giving rise to an effective nonlinear refractive index. Qiu and Penzkofer[6] calculated that the transfer of energy from the fundamental to the third-harmonic wave through the non-phase-matched second-order processes of SHG followed by SFG should be of the same order of magnitude as that due to the third-order coupling. However, the experimental uncertainties in efforts to assess this contribution[6,7] through conversion-efficiency measurements were too large for the amount of the generated light that was due to the second-order processes to be determined conclusively. In this Letter we report direct measurement of the relative contributions of $\chi^{(2)}$ and $\chi^{(3)}$ to THG in BBO for both type I and type II phase matching. Consequently, we were also able to determine the relative values for the tensor elements $\chi^{(3)}_{10}$, $\chi^{(3)}_{11}$, and $\chi^{(3)}_{16}$. Finally, conversion efficiencies to the third harmonic (355 nm) of up to 6% were obtained in a 3-mm-long crystal of BBO.

Normally, since an infinite number of interactions are possible, only the phase-matched waves are included in a calculation because the intensities of the other waves will be small. A crystal orientation for which the radiation at ω and 3ω is phase matched normally means that other processes such as SHG and SFG are not phase matched and thus not efficient. But the phase mismatch for SHG compensates for the phase mismatch for SFG (since $\Delta k_{\mathrm{SHG}} + \Delta k_{\mathrm{SFG}} = \Delta k_{\mathrm{THG}} = 0$), resulting in continual transfer of energy to the third harmonic in this cascaded process, even though the second-harmonic energy never becomes large. It then becomes necessary to include all possible interactions that can contribute to the third harmonic. As discussed by Qiu and Penzkofer, if all interactions are assumed to be independent for the case of no pump depletion, the effective nonlinear coupling to the third harmonic that is due to $\chi^{(2)}$ effects can be expressed as

$$C_{\mathrm{eff}} = \frac{2\omega d_{\mathrm{SHG}} d_{\mathrm{SFG}}}{n_{2\omega} c \Delta k_{\mathrm{SFG}}}, \tag{1}$$

where d_{SHG} and d_{SFG} are the normal effective nonlinear coupling coefficient for the SHG and the SFG portions, respectively. The overall effective coupling coefficient for THG is then given by

$$C_{\mathrm{eff}} = C^{(3)}_{\mathrm{eff}} + K \sum_{i=1}^{n} k_i C^{(2)}_{i,\mathrm{eff}}, \tag{2}$$

with $C^{(3)}_{\mathrm{eff}} = \chi^{(3)}/4$; k_i represents the degeneracy factors[10] involved in the various second-order interactions, and K is related to the inverse of the degeneracy factor for the third-order process. These factors are due to the indistinguishability of some of the waves involved in the processes, and for $o_\omega o_\omega$ SHG, $k_i = 1/2$, whereas $k_i = 1$ for other second-order processes discussed here. For type I THG, $K = 1$, and for type II THG, $K = 1/3$. In Eq. (2), the term $C^{(2)}_{i,\mathrm{eff}}$ represents the coupling that is due to all significant SHG–SFG

pairs for a given phase-matching configuration. For example, for type I THG in negative uniaxial crystals (i.e., crystal phase matched for three ordinary rays at 1ω producing one extraordinary ray at 3ω), one or all of the processes $o_\omega o_\omega \rightarrow o_{2\omega} + o_\omega o_{2\omega} \rightarrow e_{3\omega}$ and $o_\omega o_\omega \rightarrow e_{2\omega} + o_\omega e_{2\omega} \rightarrow e_{3\omega}$, as well as $o_\omega o_\omega o_\omega \rightarrow e_{3\omega}$, can be significant. Therefore, C_{eff} for type I phase matching will be

$$C_{\text{eff}}^{I} = C_{\text{eff}}^{(3)} + \frac{\omega}{c}\left(\frac{d_{\text{SHG}}^{ooo} d_{\text{SFG}}^{ooe}}{n_{2\omega}^{o}\Delta k_{\text{SFG}}^{ooe}} + \frac{d_{\text{SHG}}^{ooe} d_{\text{SFG}}^{oee}}{n_{2\omega}^{e}\Delta k_{\text{SFG}}^{oee}}\right). \quad (3)$$

For type II phase matching (i.e., crystal phase matched for $o_\omega o_\omega e_\omega \rightarrow e_{3\omega}$), the second-order processes $o_\omega o_\omega \rightarrow o_{2\omega} + e_\omega o_{2\omega} \rightarrow e_{3\omega}$, $o_\omega o_\omega \rightarrow e_{2\omega} + e_\omega e_{2\omega} \rightarrow e_{3\omega}$, $o_\omega e_\omega \rightarrow o_{2\omega} + o_\omega o_{2\omega} \rightarrow e_{3\omega}$, and $o_\omega e_\omega \rightarrow e_{2\omega} + o_\omega e_{2\omega} \rightarrow e_{3\omega}$ must all be included, and so C_{eff} is given by

$$C_{\text{eff}}^{II} = C_{\text{eff}}^{(3)} + \frac{\omega}{3c}\left(\frac{d_{\text{SHG}}^{ooo} d_{\text{SFG}}^{eoe}}{n_{2\omega}^{o}\Delta k_{\text{SFG}}^{eoe}} + \frac{d_{\text{SHG}}^{ooe} d_{\text{SFG}}^{eee}}{n_{2\omega}^{e}\Delta k_{\text{SFG}}^{eee}} + \frac{2d_{\text{SHG}}^{oeo} d_{\text{SFG}}^{ooe}}{n_{2\omega}^{o}\Delta k_{\text{SFG}}^{ooe}} + \frac{2d_{\text{SHG}}^{oee} d_{\text{SFG}}^{oee}}{n_{2\omega}^{e}\Delta k_{\text{SFG}}^{oee}}\right). \quad (4)$$

Using the fact that BBO is a uniaxial crystal and so the phase-matching angle for direct THG should be independent of the azimuthal angle ϕ, we measured the aximuthal dependence of C_{eff} by measuring the pulse energy ratio $\mathcal{E}_{3\omega}/\mathcal{E}_{\omega}^{3}$ as ϕ was varied. The sample was a 3-mm-thick piece of BBO with solgel antireflection-coated faces and an 8-mm clear aperture. The laser delivered 350-fs pulses in a 4-mm-diameter collimated beam at 1055 nm.[11] Because the phase-matching angles for type I and type II THG at the incident wavelength of 1053 nm are similar, we were able to measure the THG efficiency for both type I ($ooo \rightarrow e$, $\theta_m = 37.7°$) and type II ($ooe \rightarrow e$, $\theta_m = 47.1°$) configurations by use of the same crystal. The effective nonlinear susceptibility for type I phase matching is

$$C_{\text{eff}} = C_{10}\cos 3\phi \sin\theta_m + \frac{\omega}{c} \times \left[d_{22}^{2}\frac{\sin 6\phi}{2}\left(\frac{\cos\theta_m}{n_{2\omega}^{o}\Delta k_{\text{SFG}}^{ooe}} - \frac{\cos^3\theta_m}{n_{2\omega}^{e}\Delta k_{\text{SFG}}^{oee}}\right) + d_{22}d_{15}\cos 3\phi\left(\frac{\cos^2\theta_m \sin\theta_m}{n_{2\omega}^{e}\Delta k_{\text{SFG}}^{oee}} - \frac{\sin\theta_m}{n_{2\omega}^{o}\Delta k_{\text{SFG}}^{ooe}}\right)\right]. \quad (5)$$

Using the Sellmeier coefficients from Kato[12] and the values for $d_{22} = 2.2$ pm/V and $d_{15} = 0.16$ pm/V from Fan *et al.*,[13] we find that Eq. (5) becomes

$$C_{\text{eff}} = A\sin 6\phi + (\sin\theta_m C_{10} - B)\cos 3\phi, \quad (6)$$

with $A = 77.92\ \text{pm}^2/\text{V}^2$ and $B = 8.76\ \text{pm}^2/\text{V}^2$. The coupling that is due to the third-order susceptibility varies with ϕ as $\cos 3\phi$, with a maximum at $\phi = 0$. However, as seen in Fig. 1(a), the measured dependence has a minimum near $\phi = 0$, which indicates that the majority of the coupling in this case is due to $\chi^{(2)}$. By fitting Eq. (6) to the measured data [solid curve in Fig. 1(a)], we obtained a value for $C_{10} = \chi_{10}^{(3)}/4$ of $1.1 \times 10^{-23}\ \text{m}^2/\text{V}^2$, compared with an effective value for the cascaded second-order coupling of $8 \times 10^{-23}\ \text{m}^2/\text{V}^2$ at $\phi = -15°$.

Similarly, for type II phase matching the effective nonlinear coupling is given by

$$C_{\text{eff}} = \frac{\omega}{3c}\left\{d_{22}^{2}\left[\cos^2 3\phi\left(2\frac{\cos^4\theta_m}{n_{2\omega}^{e}\Delta k_{\text{SFG}}^{oee}} - \frac{\cos^2\theta_m}{n_{2\omega}^{o}\Delta k_{\text{SFG}}^{eoe}}\right) + \sin^2 3\phi\left(2\frac{\cos^2\theta_m}{n_{2\omega}^{o}\Delta k_{\text{SFG}}^{ooe}} - \frac{\cos^4\theta_m}{n_{2\omega}^{e}\Delta k_{\text{SFG}}^{eee}}\right)\right] - 2d_{22}d_{15} \times \sin 3\phi\left(\frac{\sin\theta_m\cos^3\theta_m}{n_{2\omega}^{e}\Delta k_{\text{SFG}}^{eee}} + \frac{\sin 2\theta_m}{n_{2\omega}^{o}\Delta k_{\text{SFG}}^{ooe}}\right) + d_{15}^{2} \times \sin^2\theta_m\left(3\frac{\cos^2\theta_m}{n_{2\omega}^{e}\Delta k_{\text{SFG}}^{eee}} + \frac{2}{n_{2\omega}^{o}\Delta k_{\text{SFG}}^{ooe}}\right) + \frac{d_{33}}{n_{2\omega}^{e}\Delta k_{\text{SFG}}^{eee}} \times (-d_{22}\sin 3\phi\cos\theta_m\sin^3\theta_m + d_{15}\sin^4\theta_m)\right\} + \left(\frac{C_{11}}{3}\cos^2\theta_m + C_{16}\sin^2\theta_m + C_{10}\sin 2\theta_m \sin 3\phi\right). \quad (7)$$

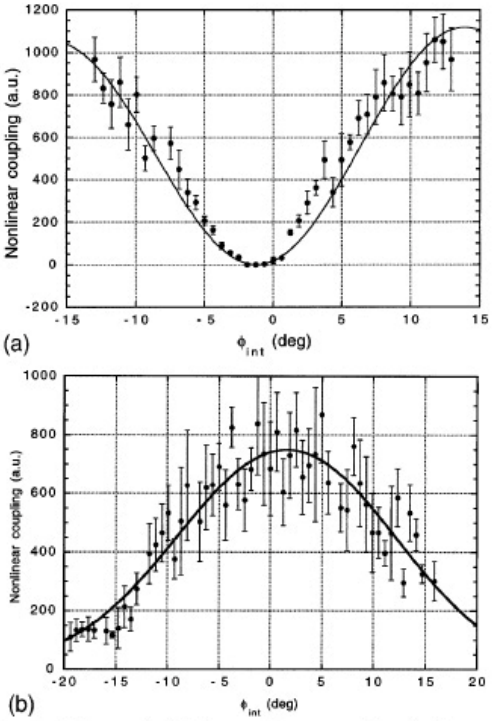

Fig. 1. Measured effective nonlinear coupling for internal azimuthal angle ϕ_{int} for (a) type I and (b) type II phase matching. The curves in (a) and (b) are the fits to the data by use of Eqs. (6) and (8), respectively.

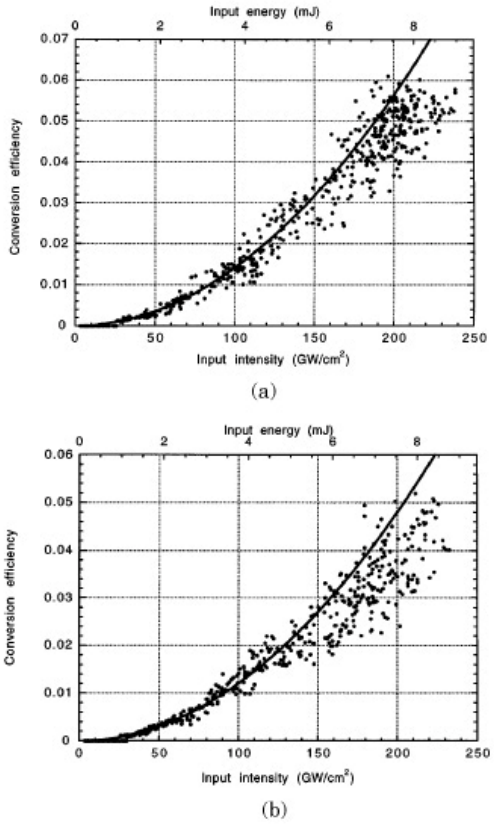

Fig. 2. Conversion efficiency ($\mathcal{E}_{3\omega}/\mathcal{E}_{\omega}$) from a single BBO crystal at 351 nm, along with a quadratic fit to low drive points. (a) Type I phase matching with $\phi_{\text{int}} = -15°$. (b) Type II phase matching with $\phi_{\text{int}} = 0°$.

After we insert the value for n, Δk, and d_{ij}, Eq. (7) becomes

$$C_{\text{eff}} = A\cos^2 3\phi + B\sin^2 3\phi + \sin 3\phi(D + Ed_{33} + 3C_{10}\sin 2\theta_m) + Fd_{33} + 3\left(\frac{C_{11}}{3}\cos^2\theta_m + C_{16}\sin^2\theta_m\right), \quad (8)$$

where $A = 49.9\ \text{pm}^2/\text{V}^2$, $B = -21.8\ \text{pm}^2/\text{V}^2$, $D = 2.0\ \text{pm}^2/\text{V}^2$, $E = -2.6$ pm/V, and $F = 0.20$ pm/V. Since $d_{15} \leq 0.1d_{22}$, the term proportional to d_{15}^2 was neglected. In this case the cubic nonlinear coupling varies as $\sin 3\phi$ and has a minimum at $\phi = 0$, but as seen in Fig. 1(b), again, there is a significant contribution from the cascaded quadratic coupling. In fitting the data with Eq. (8), we can use the value of C_{10} obtained above, but d_{33} is currently unknown and must be used as a fit parameter. We obtain a value for $(C_{11}\cos^2\theta_m)/3 + C_{16}\sin^2\theta_m$ of $4 \times 10^{-23}\ \text{m}^2/\text{V}^2$, with $d_{33} = 1.7$ pm/V. With this method, there is no way to separate the contributions of C_{11} and C_{16} further.

Finally, the conversion efficiency to the third harmonic (352 nm) from the fundamental (1055 nm) was measured for type I and type II phase matching with ϕ set to the peak of the curves shown in Fig. 1 ($\phi = -15°$ for type I and 0° for type II phase matching). The conversion efficiency as a function of input intensity is shown in Fig. 2, along with quadratic fits to the points below 100 GW/cm^2 of power. In both cases efficiencies of 5–6% were reached, and it is evident that the 3ω output is proportional to I_{ω}^3 until it is above 150 GW/cm^2.

For both type I and type II processes the azimuthal variation of the nonlinear coupling indicates that the dominant portion of the conversion to the third harmonic is due to non-phase-matched, cascaded second-order processes. In fact, for type I phase matching, the second-order coupling can be ~50× the third-order coupling. Finally, the azimuthal relationships for THG allow for direct measurement of the tensor elements of $\chi^{(3)}$ once those of the more readily measured $\chi^{(2)}$ are known.

This work was performed under the auspices of the U.S. Department of Energy by Lawrence Livermore National Laboratory under contract W-7405-ENG-48.
P. S. Banks's e-mail address is pbanks@llnl.gov.

References

1. R. W. Terhune, P. D. Maker, and C. M. Savage, Appl. Phys. Lett. **2,** 54 (1963).
2. P. D. Maker and R. W. Terhune, Phys. Rev. A **137,** 801 (1965).
3. R. C. Eckardt and C. H. Lee, Appl. Phys. Lett. **15,** 425 (1969).
4. B. C. Stuart, M. D. Feit, A. M. Rubenchik, B. W. Shore, and M. D. Perry, Phys. Rev. Lett. **74,** 2248 (1995).
5. A. Penzkofer, F. Ossig, and P. Qiu, Appl. Phys. B **47,** 71 (1988).
6. P. Qiu and A. Penzkofer, Appl. Phys. B **45,** 225 (1988).
7. I. V. Tomov, B. Van Wonterghem, and P. M. Rentzepis, Appl. Opt. **31,** 4172 (1992).
8. C. Flytzanis and N. Bloembergen, Prog. Quantum Electron. **4,** 271 (1976).
9. G. R. Meredith, J. Chem. Phys. **77,** 5863 (1982).
10. For an excellent explanation of the use of degeneracy factors in nonlinear optics, see P. N. Butcher and D. Cotter, *The Elements of Nonlinear Optics* (Cambridge U. Press, Cambridge, 1990), Chaps. 2 and 7.
11. B. C. Stuart, S. Herman, and M. D. Perry, IEEE J. Quantum Electron. **31,** 528 (1995).
12. K. Kato, IEEE J. Quantum Electron. **QE-22,** 1013 (1986).
13. Y. X. Fan, R. C. Eckardt, R. L. Byer, C. Chen, and A. D. Jiang, IEEE J. Quantum Electron. **25,** 1196 (1989).

Greg Gbur
Emil Wolf

Phase Conjugation with Random Fields and with Deterministic and Random Scatterers

Department of Physics and Astronomy, University of Rochester, New York, U.S.A

The theory of distortion correction by phase conjugation, developed since the discovery of this phenomenon many years ago, applies to situations when the field that is conjugated is monochromatic and the medium with which it interacts is deterministic. In this Letter a generalization of the theory is presented that applies to phase conjugation of partially coherent waves interacting with either deterministic or random weakly scattering nonabsorbing media.

***Keywords*: Phase conjugation, Scattering media, Nonabsorbing media**

Since the publication of a pioneering paper by Zel'dovich and collaborators,[1] the possibility of correcting various distortion effects imparted on a beam that is incident on a scattering medium by the use of the technique of phase conjugation has been confirmed by many experiments (see, for example, Refs. 2–4). The early theoretical analyses of this effect were based on the paraxial approximation[5] or on the first Born approximation.[6] Later treatments were based on more accurate analyses that took into account higher-order terms in the perturbation expansion for phase conjugation involving a broad class of scatterers.[7,8]

In all of the theoretical investigations of this subject, it was assumed that the incident field is monochromatic and that the scattering medium is deterministic. The question arises whether these assumptions can be relaxed, i.e., whether it is possible to eliminate by phase conjugation the effects of distortion imparted by the medium on the incident wave when the wave is partially coherent or when the medium is random.[9] The purpose of this Letter is to elucidate these questions.

We begin with a simpler problem, concerning the effect of phase conjugation on a partially coherent wave in free space. Consider a statistically stationary, partially coherent wave field that is incident on a phase-conjugate mirror, located in the plane $z = z_1$. For simplicity we assume that the incident field does not contain any evanescent components and that the mirror occupies the whole plane.

According to coherence theory in the space-frequency domain (Ref. 10, Sec. 4.7, especially Sec. 4.7.2), we may represent each temporal frequency component of the field in terms of an ensemble, denoted by curly brackets, $\{U(\mathbf{r},\omega)\exp(-i\omega t)\}$, of monochromatic fields, each with the same frequency ω. The phase-conjugate mirror generates a conjugate field on it surface at $z = z_1$, represented by an ensemble $\{U^{(c)}(\mathbf{r},\omega)|_{z=z_1}\exp(-i\omega t)\}$, with

$$U^{(c)}(\mathbf{r},\omega)|_{z=z_1} = \eta(\omega)U^*(\mathbf{r},\omega)|_{z=z_1}\,, \tag{1}$$

where $\eta(\omega)$ denotes the reflectivity of the phase-conjugate mirror.

It will be convenient to decompose the position vector $\mathbf{r}$ into a two-dimensional transverse vector component $\boldsymbol{\rho}$ and a longitudinal component z so that $\mathbf{r} = (\boldsymbol{\rho}, z)$ (see Fig. 1). Equation (1) then becomes

$$U^{(c)}(\boldsymbol{\rho}, z_1; \omega) = \eta(\omega)U^*(\boldsymbol{\rho}, z_1; \omega)\,. \tag{2}$$

According to a theorem derived in Ref. 11 (Theorem 6, p. 1315), one has for all $z \le z_1$,

$$U^{(c)}(\boldsymbol{\rho}, z; \omega) = \eta(\omega)U^*(\boldsymbol{\rho}, z; \omega)\,. \tag{3}$$

The physically significant quantities are, however, not the individual members U and $U^{(c)}$ of the statistical ensembles which represent the fluctuating incident and the conjugated fields, respectively, but rather their correlation functions, such as their cross-spectral densities [Ref. 10, Sec. 4.3.2 and Sec. 4.7.3, Eq. (4.7–60)],

$$W(\mathbf{r}_1,\mathbf{r}_2,\omega) = \langle U^*(\mathbf{r}_1,\omega)U(\mathbf{r}_2,\omega)\rangle\,, \tag{4a}$$

$$W^{(c)}(\mathbf{r}_1,\mathbf{r}_2,\omega) = \langle U^{(c)*}(\mathbf{r}_1,\omega)U^{(c)}(\mathbf{r}_2,\omega)\rangle\,, \tag{4b}$$

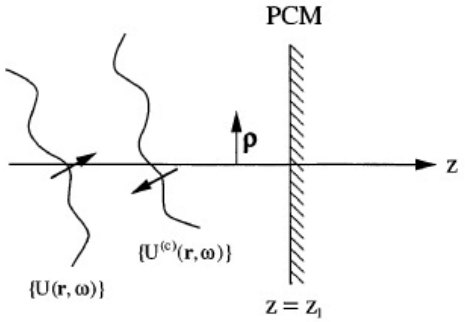

Fig. 1. Illustrating the notation relating to the behavior of waves in the vicinity of a phase-conjugate mirror (PCM). $\{U(\mathbf{r},\omega)\}$ and $\{U^{(c)}(\mathbf{r},\omega)\}$ represent the statistical ensembles characterizing the incident and the phase-conjugate field, respectively.

with the angle brackets denoting the ensemble average. It immediately follows on substituting from Eq. (3) into Eq. (4b) and using Eq. (4a) that

$$W^{(c)}(\mathbf{r}_1, \mathbf{r}_2, \omega) = |\eta(\omega)|^2 W^*(\mathbf{r}_1, \mathbf{r}_2, \omega)$$

$$\text{when } z \leq z_1 . \tag{5}$$

This relation shows that *the cross-spectral density of the conjugated field throughout the half-space $z < z_1$ is proportional to the complex conjugate of the cross-spectral density of the field incident on the phase-conjugate mirror.*[12] We note that because the cross-spectral density is Hermitian with respect to the interchange of $\mathbf{r}_1$ and $\mathbf{r}_2$ Eq. (5) may also be expressed in the form

$$W^{(c)}(\mathbf{r}_1, \mathbf{r}_2, \omega) = |\eta(\omega)|^2 W(\mathbf{r}_2, \mathbf{r}_1, \omega) . \tag{6}$$

From Eqs. (5) and (6) we may also derive a simple relation between the spectral degree of coherence (Ref. 10, Sec. 4.3.2) of the incident field,

$$\mu(\mathbf{r}_1, \mathbf{r}_2, \omega) = \frac{W(\mathbf{r}_1, \mathbf{r}_2, \omega)}{\sqrt{W(\mathbf{r}_1, \mathbf{r}_1, \omega)}\sqrt{W(\mathbf{r}_2, \mathbf{r}_2, \omega)}} , \tag{7}$$

and the spectral degree of coherence of the conjugated field,

$$\mu^{(c)}(\mathbf{r}_1, \mathbf{r}_2, \omega) = \frac{W^{(c)}(\mathbf{r}_1, \mathbf{r}_2, \omega)}{\sqrt{W^{(c)}(\mathbf{r}_1, \mathbf{r}_1, \omega)}\sqrt{W^{(c)}(\mathbf{r}_2, \mathbf{r}_2, \omega)}} . \tag{8}$$

It follows at once by making use of Eqs. (5) and (6) that

$$\mu^{(c)}(\mathbf{r}_1, \mathbf{r}_2, \omega) = \mu^*(\mathbf{r}_1, \mathbf{r}_2, \omega) \quad \text{when } z \leq z_1 \tag{9}$$

or, equivalently,

$$\mu^{(c)}(\mathbf{r}_1, \mathbf{r}_2, \omega) = \mu(\mathbf{r}_2, \mathbf{r}_1, \omega) \quad \text{when } z \leq z_1 . \tag{10}$$

At frequencies for which $\eta(\omega)$ is nonzero, Eqs. (9) and (10) are evidently independent of the mirror reflectivity. The degree of coherence of the field is, therefore, restored frequency by frequency by the phase conjugation, even though the cross-spectral density function $W(\mathbf{r}_1, \mathbf{r}_2, \omega)$ may be significantly altered in some cases.

Suppose next that a partially coherent incident field is scattered by a deterministic medium and is then phase conjugated. The conjugated field propagates back toward the medium and is also scattered by it. We will examine the relationship between the conjugated field after it has been scattered and the incident field prior to scattering. Because of the complexity of the problem we will assume that the incident and the scattered fields do not contain evanescent components and that the following additional conditions are satisfied:

(1) The scatterer is weak in the sense that the scattered field may be described, to a good approximation, by the first-order Born approximation.

(2) The scatterer is nonabsorbing.

(3) Backscattering of both the incident and the conjugated fields is negligible.

As before, we represent the incident and the conjugated field by ensembles of monochromatic realizations $\{U(\mathbf{r}, \omega)\exp(-i\omega t)\}$ and $\{U^{(c)}(\mathbf{r}, \omega)\exp(-i\omega t)\}$, respectively. Let us suppose that the scattering medium is located in the strip $0 < z < L$ and that the phase-conjugate mirror, again taken to be infinite, is located in the plane $z = z_1 > L$ (see Fig. 2). It was shown in Ref. 6, Eq. (3.4), that under the assumptions stated above, the conjugated field $U^{(c)}(\mathbf{r}, \omega)$ at any point in the half-space $z < 0$, produced from an incident monochromatic field $U(\mathbf{r}, \omega)$, are related by the equation

$$U^{(c)}(\mathbf{r}, \omega) = \eta(\omega) U^*(\mathbf{r}, \omega) , \tag{11}$$

where $\eta(\omega)$ is again the reflectivity of the phase-conjugate mirror. This equation is identical with Eq. (3), with $(\boldsymbol{\rho}, z) = \mathbf{r}$, and hence the same conclusion can be derived from it. Consequently, Eqs. (5), (6), (9), and (10) hold in the half-space $z < 0$. This result implies that *under the assumptions stated above, the presence of a deterministic scatterer in the strip $0 < z < L$ has no influence whatsoever on the partially coherent conjugated field in the half-space $z < 0$.*

Finally, let us consider the situation when the incident field is partially coherent and the scatterer is spatially random rather than deterministic but again satisfies the assumptions stated earlier. The random scatterer may be characterized by an ensemble of deterministic scatterers, and the result that we just derived will hold for each realization of the ensemble of the scatterer. Consequently, the result just stated holds not only for phase conjugation with deterministic scatterers but also with *random scatterers,* irrespective of the state of coherence of the incident field.

In the first part of this Letter we considered the effect of a phase-conjugate mirror on a partially coherent field in free space. We found simple relations between the cross-spectral density and the spectral degree of coherence of the incident field and of the conjugated field.

In the second part we considered correction by phase conjugation of distortions imparted on a partially coherent wave by scattering on a deterministic or on a random medium. We found that in both cases, provided that the scatterer is weak and nonabsorbing and that backscattering is negligible, the distortion

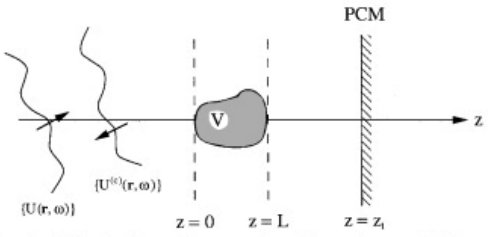

Fig. 2. Illustrating phase conjugation of a partially coherent wave scattered by a medium occupying a volume V. $\{U(\mathbf{r}, \omega)\}$ and $\{U^{(c)}(\mathbf{r}, \omega)\}$ have the same meaning as in Fig. 1.

of the incident field is completely canceled by phase conjugation.

This research was supported by the U.S. Air Force Office of Scientific Research under grants F49620-96-1-0400 and F49620-97-1-0482 and by the U.S. Department of Energy under grant DE-FG02-90ER-14119.

References

1. B. Ya. Zel'dovich, V. I. Popovichev, V. V. Ragul'skii, and F. S. Faizullov, JETP Lett. **15,** 109 (1972).
2. O. Y. Nosach, V. I. Popovichev, V. V. Ragul'skii, and F. S. Faizullov, JETP Lett. **16,** 435 (1972).
3. D. N. Bloom and C. C. Bjorklund, Appl. Phys. Lett. **31,** 592 (1977).
4. V. Wang and C. R. Giuliano, Opt. Lett. **2,** 4 (1978); R. K. Jain and R. C. Lind, J. Opt. Soc. Am. **73,** 647 (1983).
5. A. Yariv, Opt. Commun. **21,** 49 (1977).
6. G. S. Agarwal and E. Wolf, J. Opt. Soc. Am. **72,** 321 (1982).
7. G. S. Agarwal, A. T. Friberg, and E. Wolf, Opt. Commun. **43,** 446 (1982).
8. G. S. Agarwal, A. T. Friberg, and E. Wolf, J. Opt. Soc. Am. **73,** 529 (1983).
9. The effects of partial coherence on phase conjugation were recently discussed in X. Yi and P. Yeh, Opt. Commun. **147,** 126 (1998). The investigations in that paper, however, concern specific effects caused by the temporal coherence of the incident beam, not the spectral degree of coherence, which we are concerned with.
10. L. Mandel and E. Wolf, *Optical Coherence and Quantum Optics* (Cambridge University Press, Cambridge, 1995).
11. E. Wolf, J. Opt. Soc. Am. **70,** 1311 (1980).
12. A somewhat similar result was established not long ago in A. J. Devaney, A. T. Friberg, A. T. N. Kumar, and E. Wolf, Opt. Lett. **22,** 1672 (1997).

Generation of Femtosecond Pulses from Order-of-Magnitude Pulse Compression in a Synchronously Pumped Optical Parametric Oscillator Based on Periodically Poled Lithium Niobate

L. Lefort
K. Puech
S. D. Butterworth
Y. P. Svirko
D. C. Hanna

Optoelectronics Research Centre, University of Southampton, Southampton, UK

We demonstrate the generation of compressed, transform-limited 250-fs pulses, tunable in the near infrared, by means of synchronously pumped optical parametric oscillation in periodically poled lithium niobate. The almost 20-fold compression from the 4-ps pulse duration of the cw mode-locked Nd:YLF pump results in signal peak powers well in excess of the pump power.

Keywords: **Femtosecond pulses, OPO, Lithium niobate crystal**

Efficient sources of tunable coherent radiation in the near and mid infrared, in the femtosecond time domain, are necessary for many applications including spectroscopy and communications. Although synchronously pumped femtosecond optical parametric oscillators (OPO's) based on Ti:sapphire lasers routinely provide sub-100-fs pulses over a wide tuning range in the near and mid infrared,[1–3] they usually rely on either bulky ion lasers or expensive and relatively new solid-state lasers as the primary pump source. We report on the generation of tunable 250-fs pulses from an OPO synchronously pumped by a commercial, turnkey, 4-ps cw mode-locked diode-pumped Nd:YLF source ($\lambda = 1.047\ \mu$m).

All-solid-state devices that use mode-locked diode-pumped Nd lasers as the OPO pump offer practical benefits in terms of compactness and efficiency but typically produce OPO outputs in the picosecond regime, which corresponds to the pulse duration of the pump laser.[4,5] It was previously noted by a number of workers that significant pulse compression can occur in OPO's, although typically such observations have been made with high pump powers (e.g., Q-switched and mode-locked pump lasers[6,7]), thus limiting the practicality of such sources. This limitation can be overcome by exploitation of the large nonlinearity available in periodically poled lithium niobate (PPLN), which is accessible through its noncritical phase-matching capability, so high gain is achievable even with modest pump power. Here we report strong pulse compression (by almost a factor of 20) in a PPLN OPO pumped by a cw mode-locked diode-pumped Nd:YLF laser of ~1-W average power at 1.047 μm and a pulse duration of 4 ps. This laser provides a simple and practical all-solid-state source, tunable in the near infrared, that has produced nearly bandwidth-limited pulses as short as 250 fs. The compressed pulses show excellent stability, high conversion efficiency, and peak power that exceeds that of the pump.

The requirements for achieving strong pulse compression in synchronously pumped OPO's have been investigated, both experimentally and theoretically, by numerical simulations.[6–8] The results of these studies indicated a need for high parametric gain (figures of 100–1000 per pass are indicated by Khaydarov *et al.* in Ref. 7), a large group-velocity mismatch between pump and signal (resonated) pulses, and an OPO resonator slightly longer than that for exact synchronism. Typically the group-velocity mismatch should correspond to a large fraction of the pump pulse duration such that within the nonlinear crystal the signal pulse walks forward through the pump pulse by a large fraction of the pump pulse duration. This allows a signal pulse that is much shorter than the pump pulse to extract most of the pump energy and thus to have a higher peak power than the pump itself. We have replicated the above conditions in a synchronously pumped PPLN OPO and found that, in practice with a cw mode-locked pump, strong compression can be achieved with a much more modest gain; even a saturated single-pass gain of ~2 has proved sufficient. A possible explanation for the discrepancy between our results and those of Khaydarov *et al.*[7] is that they were dealing with a short (Q-switched) mode-locked pump laser envelope, so for compression to be observable in the few round trips available would have required the compression to be much stronger. In this Letter we describe the experimental results from our OPO. We have developed an analytical treatment in which pump depletion, which provides the essential pulse reshaping mechanism that leads to pulse narrowing, has been included in an approximate fashion. We have also seen good agreement with the prediction of a full numerical (plane-wave) treatment.[9]

The OPO resonator is configured as a ring (bow-tie shape; see, e.g., Ref. 10) with the output coupler mounted on a linear translation stage to vary the cavity length. The pump source is a diode-pumped additive-pulse mode-locked Nd:YLF laser of 1-W average power in 4-ps pulses at 120 MHz (Microlase DPM-100-120). An antireflection-coated 19-mm-long PPLN crystal, with periods of 30, 30.2, and 30.4 μm, was chosen to provide a group-delay difference between

the signal and the pump that was comparable with the pump pulse duration for signal wavelengths in the range 1.6–1.9 μm. Thus for a signal wavelength of 1.7 μm, for example, the calculated group-delay difference between the pump and signal is ~2.2 ps. Detailed performance measurements were made with a 15% reflectivity output coupler, thus enforcing high saturated gain operating conditions. A summary of performance data is as follows: With the OPO resonator exactly synchronous with the 120-MHz pump pulse train, the average signal power was maximum, 300 mW, at 1.7 μm for 1 W of incident pump, with an oscillation threshold of ~600 mW; the signal pulse duration was ~3 ps. Increasing the resonator length by ~20 μm (corresponding to ~70-fs delay from synchronism) gave compressed pulses of ~250 fs with slightly reduced average power of 220 mW, which corresponds to a peak power of ~7 kW, exceeding the 2-kW peak power of the pump. Typical behavior is presented in Fig. 1, which shows the output signal power (average), the pump depletion, and the observed variation in power of the second harmonic (SH) of the signal, generated extracavity, with respect to change in cavity length. Whereas the output signal power and the pump depletion have their maximum values when the OPO and pump cavities are synchronous, the SH power evidently peaks very strongly, corresponding to the signal pulse's having been compressed, when the OPO cavity length exceeds, slightly, its synchronous value. Several further experiments were performed to assess the effect of varying different parameters, e.g., output coupler reflectivity, input pump power, and signal wavelength, on the width of the compressed pulse. Compression is readily observed by use of output couplers of reflectivity that varies from 15% to 45%. The higher the reflectivity of the output coupler, the greater is the cavity mismatch required for a single compressed pulse for the same input pump power. Additionally, the greater the mismatch needed for single-pulse operation, the greater is the width of that compressed pulse. This relationship can be seen in Fig. 2, where the signal pulses obtained from use of 15%, 30%, and 45% reflective output couplers are plotted, showing an increase from ~250 to ~370 fs with increasing output coupler reflectivity. If, on the other hand, the pump power is decreased, which permits the reduction in the detuning required for a single pulse to be obtained, the pulse width decreases again. In the case of the 45% reflectivity output coupler, decreasing the power from 1 W to ~500 mW reduces the width from 370 to 250 fs. These results are consistent with the pulse width's being dependent on the pump intensity seen by the signal. In general, the shortest single pulse is obtained when one is working at a power approximately 1.5–2 times over threshold. At this power the pump depletion is ~50%. For operation close to threshold the required detuning is small, which means that the pump intensity seen by the single signal pulse is high enough to produce considerable compression. At higher powers the single pulse breaks up into two or more pulses, as shown in Fig. 3. The duration of these individual pulses can be shorter than that of the single pulse. To eliminate the satellite pulses and revert to the single-pulse situation it is necessary to increase the time mismatch.

Figure 4(a) displays the result of a typical interferometric autocorrelation of the signal pulse (output coupler reflectivity 15%, pump power 1 W) at 1.7 μm,

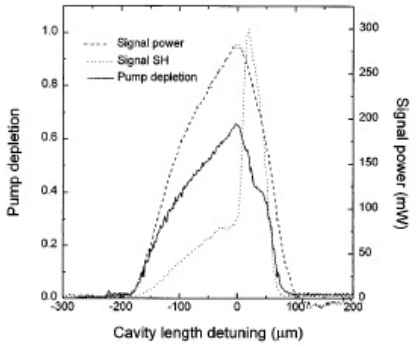

Fig. 1. Fundamental and SH power and pump depletion as a function of cavity-length detuning.

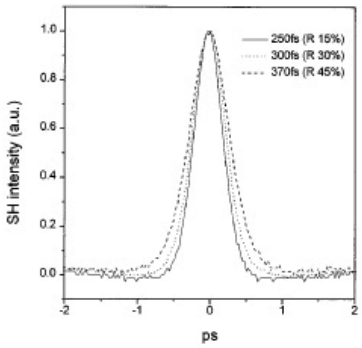

Fig. 2. Increase in compressed pulse width with increasing output coupler reflectivity for a fixed pump power of 1 W. The pulse widths are determined from a sech^2 function.

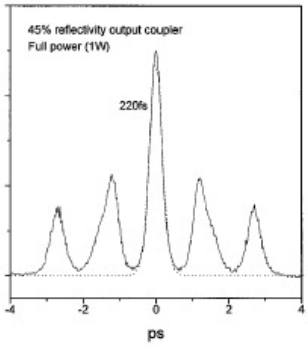

Fig. 3. Breakdown from single pulse to multiple pulses on increasing input power. Output coupler reflectivity, 45%.

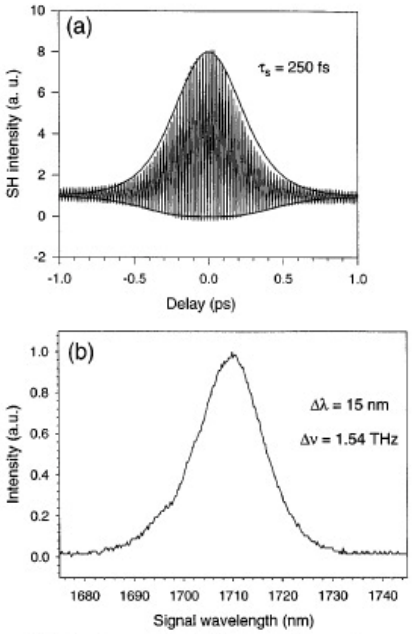

Fig. 4. (a) Interferometric SH generation autocorrelation of 250-fs signal pulses at 1.7 μm with a 15% output coupler. (b) Power spectrum of the compressed signal pulse.

for which, assuming a sech^2 fit, we deduce a width of 250 fs. In Fig. 4(b) is shown the corresponding power spectrum. The time–bandwidth product is ~0.33, indicating almost chirp-free transform-limited pulses. Similar behavior is obtained across the entire tuning range from 1.6 to 1.9 μm, with the best compression observed at 1.7 μm, and a compression factor of approximately 4–5 at 1.6 μm. Reliable and stable operation in the compressed pulse regime was observed across the spectral range.

In conclusion, we have shown that the group-velocity mismatch between signal and pump beams leads to more than an order of magnitude of compression of the signal pulses. Signal pulse compression has been observed for wavelengths from ~1.6 to ~1.9 μm. Observation of extracavity SH generation from the idler wave confirms that idler compression also occurs, although it has not been quantified.

These results demonstrate the capability of generating broadly tunable femtosecond pulses by means of OPO's based on PPLN by use of a simple compact, picosecond pump source. The same principle has been demonstrated in a Ti:sapphire-pumped OPO (not described here), for which a factor of ~5 compression was observed, yielding 400-fs signal pulses from a 2-ps pump source. No attempt at optimization was made in that event, nor is it yet clear what the appropriate combination of mirror reflectivity, pump power, and detuning should be to yield optimal compression. Detailed numerical simulations are under way to investigate this question, and we are grateful to Scroggie and co-workers[9] for producing initial results from the simulation. From them it appears that single pulses are obtained when one is working near the oscillation threshold or at a large detuning from synchronism. If these conditions are not satisfied, either the signal will consist of a train of pulses or the solutions will be nonstationary. Further research will be carried out to investigate, both theoretically and experimentally, how the compression behavior can be extended to yet shorter pulses, e.g., by use of tandem OPO's for which the output from the first pulse-compressed OPO is used as the pump source for the second one. Additionally, a detailed investigation of the extent of idler compression will be of interest.

K. Puech's e-mail address is kp@orc.soton.ac.uk.

References

1. C. L. Tang, J. Nonlin. Opt. Phys. Mater. **6,** 535 (1997).
2. C. McGowan, D. T. Reid, Z. E. Penman, M. Ebrahimzadeh, and W. Sibbitt, J. Opt. Soc. Am. B **15,** 694 (1998).
3. J. D. Kafka, M. L. Watts, and J. W. Pieterse, J. Opt. Soc. Am. B **12,** 2147 (1995).
4. S. D. Butterworth, S. Girard, and D. C. Hanna, J. Opt. Soc. Am. B **12,** 2158 (1995).
5. A. Robertson and A. I. Ferguson, Opt. Lett. **19,** 117 (1994).
6. A. Umbrasas, J.-C. Diels, J. Jacob, and A. Piskarskas, Opt. Lett. **19,** 1753 (1994).
7. J. D. V. Khaydarov, J. H. Andrews, and K. D. Singer, J. Opt. Soc. Am. B **12,** 2199 (1995).
8. J. D. V. Khaydarov, J. H. Andrews, and K. D. Singer, Opt. Lett. **19,** 831 (1994); Appl. Phys. Lett. **65,** 1614 (1994).
9. A. Scroggie, W. J. Firth, and G. L. Oppo, University of Strathclyde, Strathclyde, G1 1XQ, UK (personal communication, 1998); G. D'Allesandro, University of Southampton, Southampton, SO17 1BJ, UK (personal communication, 1998).
10. L. Lefort, K. Puech, S. D. Butterworth, G. W. Ross, P. G. R. Smith, and D. C. Hanna, Opt. Commun. **152,** 55 (1998).

IRAQI JOURNAL OF APPLIED PHYSICS

" INSTRUCTIONS TO AUTHORS "

A new Iraqi specialized quarterly periodical dedicated to publishing original papers, letters and reviews in:

Applied & Nonlinear Optics
Applied Mechanics & Thermodynamics
Digital & Optical Communications
Electronic Materials & Devices
Laser Physics & Applications
Plasma Physics & Applications
Quantum Physics & Spectroscopy
Semiconductors & Optoelectronics
Solid State Physics & Applications

CONTRIBUTIONS

Contributions to be published in this journal should be original research works, i.e., those not already published or submitted for publication elsewhere, individual papers or letters to editor.

SUBMISSION OF MANUSCRIPTS

Manuscripts should be submitted to the editor at the mailing address:

Iraqi Journal of Applied Physics
Managing Editor
P. O. Box 55259, Baghdad 12001, IRAQ
irq_appl_phys@yahoo.com

Iraqi Journal of Applied Physics
Editor-In-Chief
P. O. Box 55159, Baghdad 12001, IRAQ
editor_ijap@yahoo.co.uk

MANUSCRIPTS

Two copies with soft copy on a compact disc (CD) should be submitted to Editor in the following configuration:

- Double-spaced one-side A4 size with 2.5 cm margins of all sides
- 12pt Times New Roman font
- Letters should not exceed 5 pages, papers no more 20 pages and reviews are up to author.
- Manuscripts presented in English only are accepted.
- Authors confirm affiliations, addresses and emails. Email is necessary for correspondences.
- English abstract not exceed 150 words
- 4 keywords (at least) should be maintained on (PACS preferred)
- Author(s) should express all quantities in SI units
- Equations should be written in equation form (italic and symbolic)
- Figures and Tables should be separated from text
- Figures and diagrams can be submitted in colors for assessment and they will be returned to authors after provide printable copies
- Charts should be indicated by the software used for
- Only original or high-resolution scanner photos are accepted
- References are written in titles, full-name authors, names of publications, years, volumes, issues and pages (from-to)

PROOFS

Authors will receive proofs of papers and are requested to return one corrected hard copy with a WORD copy on a compact disc (CD). New materials inserted in the original text without Editor permission may cause rejection of paper.

COPYRIGHT FORM

Author(s) will be asked to transfer copyrights of the article to the Journal soon after acceptance of it. This will ensure the widest possible dissemination of information.

OFFPRINTS

Authors will receive offprints free of charge and any additional offprints can be ordered.

SUBSCRIPTION AND ORDERS

Annual fees (4 issues per year) of subscription are:

50 000 Iraqi dinars for individuals and establishments inside Iraq.
50 US$ for individuals and establishments abroad.

Fees are reduced by 25% for I.S.A.R.E.S.T. members. Orders of issues can be submitted by contacting the editor-in-chief or editorial secretary to maintain the address of issue delivery and payment way.

THE IRAQI JOURNAL OF APPLIED PHYSICS
EDITORIAL BOARD
P. O. Box 55259, Baghdad 12001, IRAQ
Email: editor_ijap@yahoo.com

COPYRIGHY RELEASE

Iraqi Journal of Applied Physics (IJAP)

We, the undersigned, the author/authors of the article titled

……
……
……
……
……
……

that is presented to the Iraqi Journal of Applied Physics (IJAP) for publication, declare that we have neither taken part or full text from any published work by others, nor presented or published it elsewhere in any other journal. We also declare transferring copyrights and conduct of this article to the Iraqi Journal of Applied Physics (IJAP) after accepting it for publication.

The authors will keep the following rights:

1. **Possession of the article such as patent rights.**
2. **Free of charge use of the article or part of it in any future work by the authors such as books and lecture notes without referring to the IJAP.**
3. **Republishing the article for any personal purposes of the authors after taking journal permission.**

To be signed by all authors:

Signature:……..date: ……..

Printed name: ……

Signature:……..date: ……..

Printed name: ……..

Signature:……..date: ……..

Printed name: ……..

Correspondence address:

……
……
……
Address:……
……
……
Telephone:……..email: ……..

Note: Please complete and sign this form and mail it to the below address with your manuscript

The Iraqi Journal of Applied Physics,
P. O. Box 55259, Baghdad 12001, IRAQ
Email: *irq_appl_phys@yahoo.com* OR *editor_ijap@yahoo.co.uk*, Mobile: +964-7901274190

Vol. 2 , No. 3-4 , July-October , 2006

IRAQI JOURNAL OF APPLIED PHYSICS

CONTENTS